

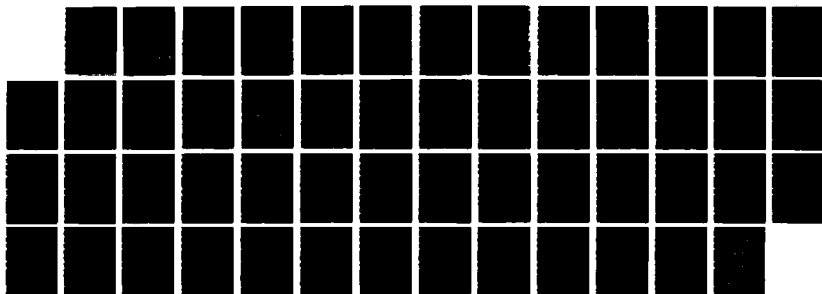
ND-A187 716

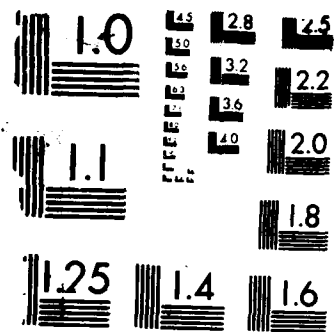
DETERMINATION OF THE ULTIMATE LOADS FOR
CORRUGATED-STEEL BARREL-TYPE SHELL STRUCTURES(U)
CONSTRUCTION ENGINEERING RESEARCH LAB (ARMY) CHAMPAIGN
IL D BRIASSOULTS ET AL OCT 87

171

UNCLASSIFIED

F/G 13/13 NL





MICROCOPY RESOLUTION TEST CHART



US Army Corps
of Engineers
Construction Engineering
Research Laboratory

USA-CERL TECHNICAL REPORT M-88/01
October 1987
Rapidly Erectable Lightweight Mobilization Structures

DTIC FILE COPY

AD-A187 716

Determination of the Ultimate Loads for Corrugated-Steel, Barrel-Type Shell Structures

by
Demetres Briassoulis
Anthony Kao
Steven Sweeney

To meet the increased need for facilities during mobilization, new construction technologies have been developed. However, conventional design procedures (e.g., for ultimate loads) may not apply to these structures.

In this report, the ultimate snow and wind loads are determined for two sizes of a corrugated-steel, barrel-type shell building by using numerical and experimental methods. Local buckling is shown to govern the ultimate loading of these structures, through the formation of collapsing mechanisms. The critical positive and negative moment fields under which hinges are formed determine the bounds to the critical loads which will create the collapsing mechanisms. The lower bounds of the ultimate snow load for the intermediate (50 ft wide by 18 ft high) and large (72 ft wide by 26 ft high) structures were found to be 35 psf and 14 psf, respectively. The ultimate wind velocities for the same intermediate and large structures were 87 to 110 mph and 60 to 74 mph, respectively. Although methods and assumptions used in the analysis are considered conservative, it does indicate that with respect to wind loading, some existing structures may be operating at or near ultimate strength.

DTIC
ELECTE
DEC 21 1987
S OSH D

The contents of this report are not to be used for advertising, publication, or promotional purposes. Citation of trade names does not constitute an official indorsement or approval of the use of such commercial products. The findings of this report are not to be construed as an official Department of the Army position, unless so designated by other authorized documents.

*DESTROY THIS REPORT WHEN IT IS NO LONGER NEEDED
DO NOT RETURN IT TO THE ORIGINATOR*

UNCLASSIFIED

SECURITY CLASSIFICATION OF THIS PAGE

REPORT DOCUMENTATION PAGE				Form Approved OMB No 0704 0188 Exp Date Jun 30 1986	
1a REPORT SECURITY CLASSIFICATION UNCLASSIFIED			1b RESTRICTIVE MARKINGS A187716		
2a SECURITY CLASSIFICATION AUTHORITY			3 DISTRIBUTION / AVAILABILITY OF REPORT Approved for public release; distribution is unlimited.		
2b DECLASSIFICATION DOWNGRADING SCHEDULE			5 MONITORING ORGANIZATION REPORT NUMBER(S)		
4 PERFORMING ORGANIZATION REPORT NUMBER(S) USA-CERL TR M-88/01			7a NAME OF MONITORING ORGANIZATION		
6a NAME OF PERFORMING ORGANIZATION U.S. Army Construction Engr Research Laboratory		6b OFFICE SYMBOL (If applicable)		7b ADDRESS (City, State, and ZIP Code)	
6c ADDRESS (City, State, and ZIP Code) P.O. Box 4005 Champaign, IL 61820-1305			9 PROCUREMENT INSTRUMENT IDENTIFICATION NUMBER		
8a NAME OF FUNDING SPONSORING ORGANIZATION Office of the Chief of Engr		8b OFFICE SYMBOL (If applicable) DAEN-ZCM		10 SOURCE OF FUNDING NUMBERS	
8c ADDRESS (City, State, and ZIP Code) The Pentagon Washington, D.C. 20310-2600			PROGRAM ELEMENT NO 4A162731	PROJECT NO AT41	WORK UNIT ACCESSION NO 079
11 TITLE (Include Security Classification) Determination of the Ultimate Loads for Corrugated-Steel, Barrel-Type Shell Structures (Unclassified)					
12 PERSONAL AUTHOR(S) Briassoulis, Demetres; Kao, Anthony; Sweeney, Steven					
13a TYPE OF REPORT Final		13b TIME COVERED FROM _____ TO _____		14 DATE OF REPORT (Year Month, Day) October 1987	
15 PAGE COUNT 51					
16 SUPPLEMENTARY NOTES Copies are available from the National Technical Information Service Springfield, VA 22161					
17 COSATI CODES			18 SUBJECT TERMS (Continue on reverse if necessary and identify by block number)		
FIELD 13	GROUP 13	SUB-GROUP	K-Span buildings, shells (structural forms) snow loads wind loads		
19 ABSTRACT (Continue on reverse if necessary and identify by block number) To meet the increased need for facilities during mobilization, new construction technologies have been developed. However, conventional design procedures (e.g., for ultimate loads) may not apply to these structures. In this report, the ultimate snow and wind loads are determined for two sizes of a corrugated steel, barrel-type shell building by using numerical and experimental methods. Local buckling is shown to govern the ultimate loading of these structures, through the formation of collapsing mechanisms. The critical positive and negative moment fields under which hinges are formed determine the bounds to the critical loads which will create the collapsing mechanisms. The lower bounds of the ultimate snow load for the intermediate (50 ft wide by 18 ft high) and large (72 ft wide by 26 ft high) structures were found to be 35 psf and 14 psf, respectively. The ultimate wind velocities					
20 DISTRIBUTION AVAILABILITY OF ABSTRACT <input type="checkbox"/> UNCLASSIFIED / UNLIMITED <input checked="" type="checkbox"/> SAME AS RPT <input type="checkbox"/> DTIC USERS			21 ABSTRACT SECURITY CLASSIFICATION UNCLASSIFIED		
22a NAME OF RESPONSIBLE INDIVIDUAL Jane Andrew			22b TELEPHONE (Include Area Code) (217) 352-6511 (x388)		22c OFFICE SYMBOL CECER-IMT

(Cont'd)

UNCLASSIFIED

BLOCK 19 (Cont'd)

for the same intermediate and large structures were 87 to 110 mph and 60 to 74 mph, respectively. Although methods and assumptions used in the analysis are considered conservative, it does indicate that with respect to wind loading, some existing structures may be operating at or near ultimate strength. *(Key words →)*

UNCLASSIFIED

FOREWORD

This research was performed for the Office of the Chief of Engineers (OCE) under Project 4A162731AT41, "Military Facilities Engineering Technology"; Task Area E, "Military Engineering"; Work Unit 079, "Rapidly Erectable Lightweight Mobilization Structures."

The research was performed by the Engineering and Materials Division (EM), U.S. Army Construction Engineering Research Laboratory (USA-CERL). The OCE Technical Monitor was Mr. Austin Owen (DAEN-ZCM). USA-CERL personnel directly involved in the study were Mr. Steven Sweeney and Dr. Anthony Kao, Team Leader of the Construction and Maintenance Team. Dr. D. Briassoulis is a Visiting Assistant Professor at the University of Illinois, Urbana.

Dr. Robert F. Quattrone is Chief of EM. COL Norman C. Hintz is Commander and Director of USA-CERL, and Dr. L. R. Shaffer is Technical Director.



Accession For	
NTIS GRA&I	<input checked="checked" type="checkbox"/>
DTIC TAB	<input type="checkbox"/>
Unannounced	<input type="checkbox"/>
Justification	
By	
Distribution/	
Availability Codes	
Avail and/or	
Dist	Special
A-1	

CONTENTS

	Page
DD FORM 1473	1
FOREWORD	3
LIST OF TABLE AND FIGURES	5
1 INTRODUCTION	7
Background	
Objective	
Approach	
Scope	
Mode of Technology Transfer	
2 LOADING	9
Wind Loading	
Snow Loading	
3 MODELING THE CORRUGATED SHELL STRUCTURE	11
Structures Being Modeled	
Equivalent Orthotropic Properties	
Finite Element Models	
Comparing the Two Models	
4 OVERALL BUCKLING AND LOCALIZED NONLINEARITIES	18
Large Building	
Intermediate Building	
Localized Nonlinearities	
5 CRITICAL MOMENTS AND LOCAL BUCKLING	25
Critical Moments	
Cantilever Panel-Beam	
The Simply Supported Panel-Beam	
Critical Negative Moments	
Local Buckling Considerations	
Approximate Analytical Formulas	
Arch Structure Under a Line Load	
Summary of Critical Moment Bounds	
6 COLLAPSING MECHANISMS AND ULTIMATE LOADS	41
Balanced Snow Load—Intermediate Building	
Balanced Snow Load—Large Building	
Unbalanced Snow Load—Intermediate Building	
Unbalanced Snow Load—Large Building	
Wind Load	
The Effect of Higher Critical Negative Moments	
7 CONCLUSIONS	48
METRIC CONVERSION FACTORS	49
REFERENCES	50
DISTRIBUTION	

TABLE

Number		Page
1	Equivalent Orthotropic Properties of a Typical Curved Panel	12

FIGURES

1	Geometric Characteristics of the Barrel Shell	10
2	Dimensions of Corrugated Profile of a Typical Curved Panel	15
3	Cross-Section of an Arch Panel Showing Minor Corrugations	15
4	Finite Element Mesh Used for the Orthotropic Model With 9-Node Lagrangian Elements	16
5	Section of the Detailed Model Used With 16-Node Lagrangian Elements	16
6	Deformation Patterns of the 72 by 26 ft Building Obtained by the Orthotropic and the Models	17
7	Typical Stress Distribution in the Cross Section at the Base of the Structure Obtained by the Detailed Model	17
8	Nonlinear Behavior of the Large Building Under Balanced Snow Loading, Assuming Symmetric Mode With Fixed Base	21
9	Nonlinear Behavior of the Large Building Under Balanced Snow Loading, Assuming Antisymmetric Mode With Hinged Base	22
10	Nonlinear Behavior of the Large Building Under Unbalanced Snow Loading	22
11	Nonlinear Behavior of the Large Building Under Wind Loading	23
12	Nonlinear Behavior of the Intermediate Building Under Balanced Snow Loading, Assuming Symmetric Mode With Fixed Base	23
13	Nonlinear Behavior of the Intermediate Building Under Balanced Snow Loading, Assuming Antisymmetric Mode With Hinged Base	24
14	Nonlinear Behavior of the Intermediate Building Under Unbalanced Snow Loading	24
15	Typical Simply Supported Panel-Beam Under Two Concentrated Loads Applied Downward and Upwards, Tested in a Series of Full-Scale Tests, and Analyzed Numerically	35

FIGURES (Cont'd)

Number		Page
16	Nonlinear Analysis and Full-Scale Tests Results of a Straight Panel-Beam, Loaded Downward	35
17	Stress Distribution in a Section of the Straight Panel According to the Numerical Analysis and the Full-Scale Tests	36
18	Lateral-Local Buckling of the Straight Beam in the Presence of Initial Imperfections (Numerical Analysis)	36
19	Nonlinear Analysis and Full-Scale Test Results of a Straight Panel-Beam, Loaded Upwards	37
20	Nonlinear Analysis and Full-Scale Test Results of a Curved Panel-Beam, Loaded Downward	38
21	Stress Distribution in the Curved Panel With and Without Minor Corrugations, Modeled With Isotropic and Orthotropic Shell Elements, Respectively	39
22	Nonlinear Analysis and Full-Scale Test Results of a Curved Panel-Beam, Loaded Upwards	39
23	Numerical Analysis and Full-Scale Test Results of the Arch Structure Under a Line Load	40
24	Moment Distribution in Half of the Arch Structure Before and After the Formation of the First Hinge, Corresponding to the Critical Positive and Negative Moment Fields, Respectively	40
25	Moment Distribution in the Intermediate Building Under the Reference Balanced Snow Loading	44
26	Collapsing Mechanisms for the Intermediate (a-b) and the Large (c-e) Buildings, Under Balanced (a,c), Unbalanced (b,d), and Wind Loading (e)	45
27	Moment Distribution in the Large Building Under the Reference Balanced Snow Loading	46
28	Moment Distribution in the Intermediate Building Under the Reference Unbalanced Snow Loading	46
29	Moment Distribution in the Large Building Under the Reference Unbalanced Snow Loading	47
30	Moment Distribution in the Large Building Under the Reference Wind Loading	47

DETERMINATION OF THE ULTIMATE LOADS FOR CORRUGATED-STEEL, BARREL-TYPE SHELL STRUCTURES

1 INTRODUCTION

Background

Mobilization planners have identified that a serious shortage of facilities would occur in the event of full mobilization. Based on the 1980 report "Corps Mobilization Capabilities, Requirements, and Planning,"¹ peak continental United States (CONUS) troop strength would occur as early as day M + 28. The need therefore exists to identify construction technologies which can be used to satisfy mobilization.

One solution to this problem is using buildings constructed on-site by special building systems. One such system, the K-Span multipurpose building system, is being evaluated as a rapidly erectable lightweight mobilization structure (RELMS). The system consists of lightweight, cold-rolled steel channels formed on-site from coil stock into circular arch shapes of various widths and heights. Details of the construction and materials are given in K-Span's *Metal Building Data Manual*.² A demonstration of the system by the machine manufacturer has shown that a 12-man crew can construct 5,000 sq ft* of bare structure (no utilities) in 12 hours.

Because of the unique configuration of the cold-rolled arch sections and the seaming process used to produce the building shell, conventional design procedures based on standard specifications may not be appropriate. A more specific method for determining the load bearing capabilities is required.

Objective

The objective of this study was to determine the collapse loads of corrugated-steel barrel-type shells (K-Span buildings), under snow and wind loading conditions. The researchers studied the effect of the geometry of the structure and of localized nonlinearities (i.e., local buckling and yielding) on the mode of failure and the corresponding collapse loads.

Approach

Two buildings were studied, one medium-sized (50 ft wide by 18 ft high) and one large (72 ft wide by 26 ft high). These were assumed to be long shells so that the effects of the end walls³ could be ignored.⁴ (The behavior of barrel-type shells depends very

¹U.S. Army Engineer Studies Center, "Corps Mobilization Capabilities, Requirements, and Planning" (Corps of Engineers, March 1980).

²K-Span, *Metal Building Data Manual* (G. A. Kundson Ltd., Washington, DC).

*Metric conversion factors are provided on p 49.

³K-Span.

⁴M. N. El-Atrouzy and G. Abdel-Sayed, "Prebuckling Analysis of Orthotropic Barrel-Shells," *American Society of Civil Engineers Proceedings, Journal of the Structural Division*, Vol 104, ST11 (1978), pp 1775-1786.

much on the aspect ratio, length/radius.⁵) This assumption makes it possible to use simpler models for numerical nonlinear analysis.

Expressions for wind and snow loading conditions were taken from American National Standards Institute (ANSI) Standard A58.1⁶ (Chapter 2). Equivalent orthotropic properties were developed for the structures, along with two finite element models, one orthotropic and one detailed. In a comparative linear elastic analysis, the detailed model was used to verify the orthotropic model (Chapter 3). In a preliminary analysis, the orthotropic model was used to determine the overall buckling behavior of the structures and to find out if local buckling and other localized nonlinearities would have a significant effect on their strength (Chapter 4). In Chapter 5, sections of the structures were treated as simple beams, and the detailed finite element model was used to determine the upper and lower bounds of the critical moments which will result in localized nonlinearities. These results were compared to those of full-scale tests performed on the same sections. (The full-scale tests will be discussed in detail in another report.) An arch section of the structure under a line load was also analyzed numerically with the orthotropic model. The critical moments obtained earlier were used to determine the formation of hinges and the corresponding collapse mechanism. These results were verified by full-scale tests of the same arch section. Finally in Chapter 6, collapse mechanisms and the corresponding ultimate loads were determined. The critical moments obtained earlier were the basis for the critical bounds to the ultimate wind and snow loads.

The numerical analyses carried out in the course of this study were performed on the Harris-800 computer at the Department of Civil Engineering of the University of Illinois (UI). In some cases, the UI CDC-175 mainframe system of the UI was also used. The two finite element analysis programs used were POLO-FINITE⁷ and Automatic Dynamic Incremental Nonlinear Analysis (ADINA).⁸

Scope

In the present study, only two structures were analyzed; the largest available K-Span structure and an intermediate one. It is assumed that the factors governing the collapse of these buildings will apply to K-Span buildings of any size. Also, the results obtained are applicable only to the particular corrugation profile that was analyzed.⁹

Mode of Technology Transfer

Results of this study are to be transferred to Corps of Engineers district offices and other Army installations through Technology Transfer Test Bed programs.

⁵D. P. Billington, Thin Shell Concrete Structures, 2nd ed. (McGraw-Hill, NY, 1982).

⁶ANSI Standard A58.1, Minimum Design Loads for Buildings and Other Structures (American National Standards Institute, Inc., NY, 1982).

⁷L. A. Lopez, "FINITE: An Approach to Structural Mechanics System," International Journal of Numerical Methods in Engineering, Vol 11 (1977), pp 851-866.

⁸K.J. Bathe, A Finite Element Program for Automatic Dynamic Incremental Nonlinear Analysis, Report 82448.1 (Acoustics and Vibration Laboratory, Department of Mechanical Engineering, Massachusetts Institute of Technology, Cambridge, MA, 1975 [rev. 1978]).

⁹K-Span.

Snow Loading

Two cases of snow loading are considered: snow not combined with wind (balanced or symmetric), and snow combined with wind (unbalanced or nonsymmetric). The snow loading on sloped-roof structures is given by ANSI for $\alpha < 70$ degrees (Figure 1), by:

$$p_s = C_s p_f \quad [\text{Eq 2}]$$

where C_s is the roof slope factor, given by Figure 8 of ANSI Standard A58.1 for warm and cold roofs, as a function of the roof slope. The flat-roof snow load p_f is given by:

$$p_f = 0.7 C_e C_t I p_g \quad [\text{Eq 3}]$$

where C_e = exposure factor

C_t = thermal factor

I = importance factor

p_g = ground snow load.

C_e was assumed to be 1.2 for the balanced snow loading and 0.80 for the unbalanced snow loading.¹¹ The structure was also assumed to be unheated, with $C_t = 1.2$, the importance factor was assumed to be 1, and the reference ground snow load was taken as $p_g = 100$ psf. The unbalanced snow loading distribution for curved roofs is determined from Figure 10 of ANSI Standard A58.1.

The snow load analyses in this report are concerned with determining a structure's reaction to the ground snow load. This load is expressed as a ratio of the actual ground snow load to the reference load of 100 psf.

¹² ANSI A58.1.

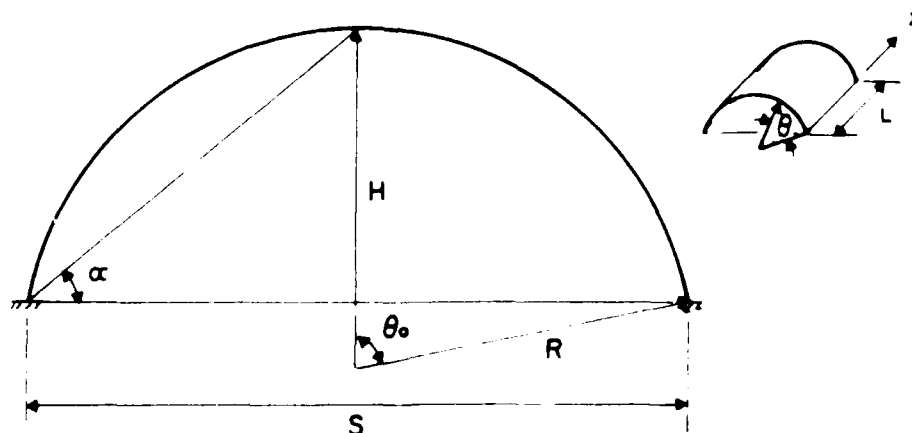


Figure 1. Geometric characteristics of the barrel shell.

3 MODELING THE CORRUGATED SHELL STRUCTURE

In this chapter two models are developed. The first is an orthotropic finite element model of the corrugated shell structure. This model is used in following chapters for nonlinear analysis for large deformations. Localized nonlinearities (local buckling or yielding) cannot be considered in a nonlinear analysis using this model. Therefore, the second model, a detailed finite element model of the "details" of the corrugated panel, is developed. This model will be used later to analyze the typical corrugated panel for localized nonlinearities. The detailed model is used in the present chapter, only to test the orthotropic model through a comparative linear elastic analysis.

Structures Being Modeled

Two buildings were selected for this analysis. One is a large building, 72 ft wide by 26 ft high, constructed using material having a thickness of 0.035 in. This building, since it is the largest available example of the category of structures under investigation, was selected to determine the limiting buckling behavior of this type of structure. The second structure is an intermediate sized building 50 by 18 ft of the same thickness as the large one. This is considered to be a representative size for this type of building.¹³

Equivalent Orthotropic Properties

To analyze a corrugated shell structure as an equivalent orthotropic shell, one must use the equivalent orthotropic properties of the corrugated sheet. Figure 2 presents the geometric characteristics of a typical section of the curved panel used in the construction of the K-Span structures. This section is not a standard corrugated profile (e.g., tangent-and-arc), so the equivalent orthotropic properties were derived in the course of this study. The derivation of the equivalent orthotropic properties of the typical section was based on the approach used by Briassoulis for standard corrugated profiles.¹⁴ That approach is based on Castigliano's second theorem and has been confirmed with a finite element analysis to yield equivalent orthotropic properties which, in some cases, improve the older expressions found in the literature. The real curved panel has, in addition, some minor corrugations which run across the width of the flange and web sections of the panel. These minor corrugations were not included in the derivation of the equivalent orthotropic properties of the curved panel. Their effect is studied later in this report. The orthotropic model is therefore based on the idealized, typical section of the panel shown in Figure 3 (minor corrugations ignored, ridge assumed symmetric), which, nevertheless, is a type of nonstandard corrugated profile.

The derived equivalent orthotropic rigidities of the corrugated profile of Figure 2 are presented in Table 1. As expected, the major effect of the corrugations is the decrease of the meridional extensional rigidity and the increase of the circumferential flexural rigidity.

¹³K-Span.

¹⁴D. Briassoulis, "Analysis of the Behavior of Steel Silos Under Wind Loading," Ph.D. Dissertation, University of Illinois, Urbana, 1985; D. Briassoulis, "Equivalent Orthotropic Properties of Corrugated Sheets," *International Journal of Computers and Structures*, Vol 23, No. 2 (1985), pp 129-138.

Table 1

Equivalent Orthotropic Properties of a Typical Curved Panel

$$tE_x = \frac{tE}{1 + \left[\left(\frac{e}{s} \right)^2 + \frac{2}{t} \frac{f}{\pi} \frac{e}{t} \frac{s}{c} (1 - \cos \frac{\pi s}{c}) + \frac{f^2}{2t^2} \left(\frac{s}{c} \right)^2 - \frac{s}{2\pi c} \sin \frac{2\pi s}{c} + \frac{2}{3} \frac{b}{c} \left(\frac{b}{t} \right) \left(\left(1 - \frac{e}{b} \right)^3 + \left(\frac{e}{b} \right)^3 \right) \right] 12(1-\mu)}^2$$

$$tE_\theta = tE \frac{1}{c}$$

$$tE_{x\theta} = \frac{tE}{2(1+\mu)}$$

$$B_x = \frac{Et^3}{12(1-\mu^2)} \frac{c}{l}$$

$$B_\theta = \frac{Et^3}{12(1-\mu^2)} + Et^3 \left[\left(\frac{e}{t} \right)^2 + \frac{\mu e f}{nt^2} + \frac{f^2}{2t^2} + \frac{(b-e)^2 \mu a}{t^2 c} + \frac{2}{3} \left(\frac{b-e}{ct^2} \right)^3 + \frac{e^3}{ct^2} \right]$$

$$B_{x\theta} = \frac{Et^3}{24(1+\mu)}$$

$$\text{where: } s = \frac{2\pi r_\theta}{360}, e_o = r_\theta \left(\frac{\pi \theta}{c} \cos(90 - \frac{\theta}{c}) - \cos \frac{\theta}{2} \right), e = \frac{b^2 + \mu ab - se_o}{s + 2b + \mu a}, l = s + 2b$$

Finite Element Models

Two models of the 72 by 26 ft building were employed. An orthotropic model (Figure 4) and a detailed model (Figure 5) of an isolated strip of the structure were both obtained by imposing conditions of symmetry according to the assumption of a long shell. That is, the typical strip of the structure under consideration is assumed to be away from the end walls and to represent the buckling behavior of a corresponding long structure ($L/R > 4$).

The 9 node, orthotropic, Lagrangian degenerated shell element¹⁵ was used with the orthotropic model. Fourteen elements were used as shown in Figure 4. Reduced integration was employed throughout this study because full integration results in locking mechanisms when used with very thin elements, producing over stiff structures.¹⁶ Zero energy modes, which constitute the most serious problem when reduced integration is employed, did not arise in any of the analyses of this study, probably because of the many constraints present at the boundaries of the model (symmetry lines and fixed bases).

The detailed model was built using thirty 16-node Lagrangian degenerated elements using the program ADINA.¹⁷ The seam between the two panels was assumed to be symmetric (Figure 5). The behavior of the seam was approximated by 4-node truss elements because of problems encountered in using compatible beam elements (probably due to the extreme thickness to length ratio of the ridge-beam elements).

The detailed model was considered to be necessary in this phase for testing the performance of the orthotropic model and was used only with the large 72 by 26 ft building in a linear elastic comparative analysis. This analysis was done under balanced snow loading; thus, due to symmetry, it was only necessary to model half the arch.

Comparing the Two Models

Figure 6 presents the deformation patterns obtained from the orthotropic and the detailed models, under a balanced snow loading $p_g = 90$ psf. The response of the equivalent orthotropic model seems to be very good, resulting in a midspan deflection of 6.19 in. versus 6.32 in. obtained by the detailed model. This 2 percent difference is probably due to several factors: the two meshes are different; several assumptions were made in the detailed model (such as the use of an average normal vector at the junction of the two 16-node elements (Figure 5); and it was difficult to impose conditions of symmetry in the case where the rotational nodal unit vectors did not correspond to the directions of the global coordinates.¹⁸

For vertical reaction at the base of the structure, the orthotropic model gave 285 lb/in. and the detailed model gave 286 lb/in., compared to the analytically obtained value of 283 lb/in. The typical stress distribution in the cross section at the base region of the detailed model is shown in Figure 7. The corrugated profile actually behaves as a one-

¹⁵D. Briassoulis, Ph.D. dissertation; H. Parish, "A Critical Survey of the Nine-Node Degenerated Shell Element With Special Emphasis on Thin Shell Application and Reduced Integration," *Computer Methods in Applied Mechanical Engineering*, Vol 20 (1979), pp 323-350; L. A. Lopez.

¹⁶H. Parish.

¹⁷K. J. Bathe.

¹⁸K. J. Bathe.

way beam section, with linear distribution of stress and strain. Note that this behavior is the basis for the derivation of the circumferential flexural rigidity of the orthotropic model (Table 1).

The fiber stress of the section can be obtained by using the equivalent orthotropic properties of Table 1, as follows:

$$\sigma_{\theta} = \frac{cN_{\theta}}{t\ell} + \frac{EM_{\theta}y}{B_{\theta}} \quad [\text{Eq 4}]$$

where c = projected length of the panel profile

N_{θ} = circumferential stress resultant

E = modules of elasticity of the material

M_{θ} = circumferential moment

y = distance from the neutral axis to the fiber (Figure 2)

t = thickness of sheet

ℓ = developed length of the panel profile

B_{θ} = circumferential bending rigidity as defined in Table 1.

The stresses at the base of the structure obtained by Equation 4 were found to be in a good agreement with the results of the detailed model. Given the good agreement between the responses obtained from the two models, the orthotropic model, which uses the equivalent properties presented in Table 1, is verified.

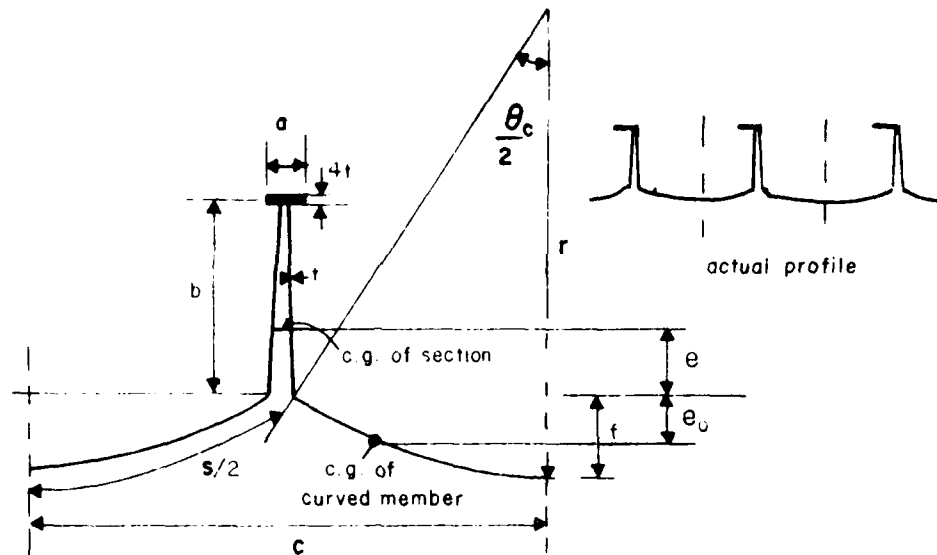


Figure 2. Dimensions of corrugated profile of a typical curved panel (from K-Span, *Metal Building Data Manual* [G. A. Knudson, Ltd., Washington, DC]).

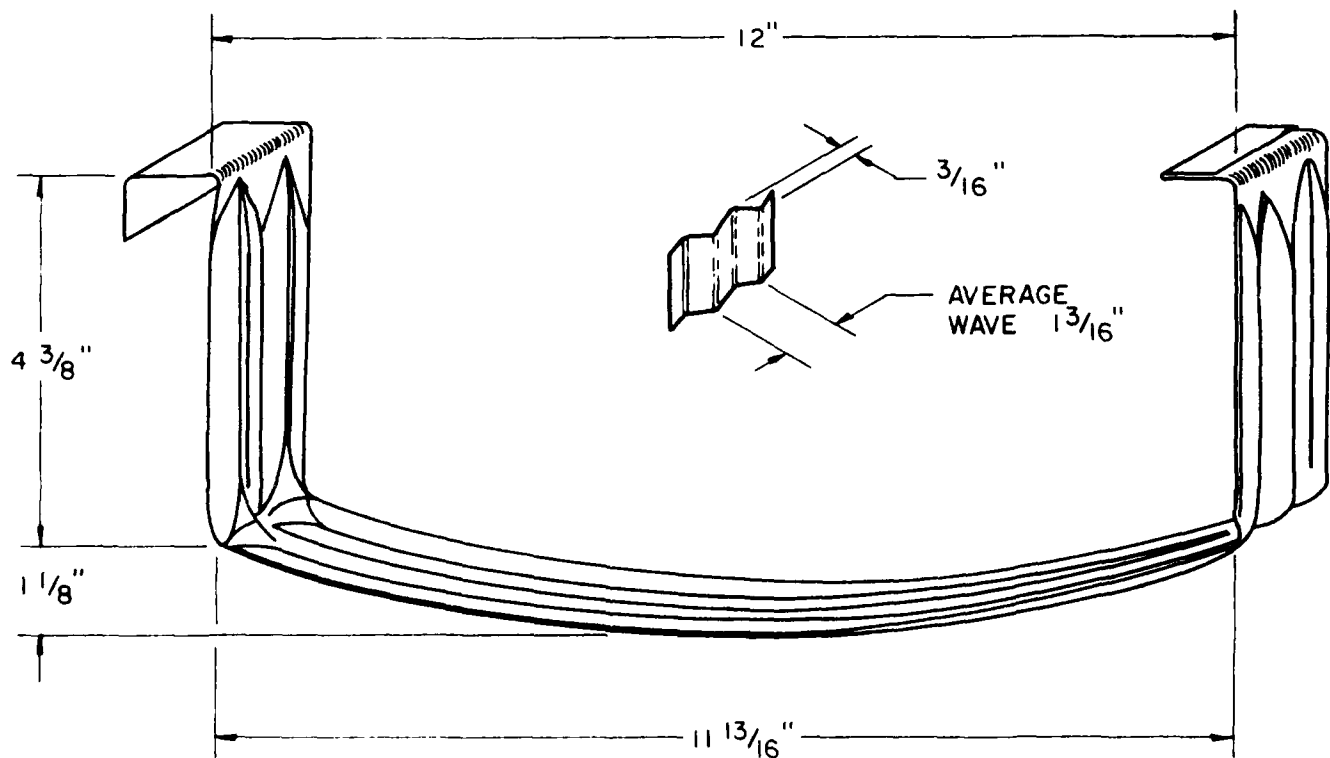


Figure 3. Cross section of an arch panel showing minor corrugations (from K-Span, *Metal Buildings Data Manual* [G. A. Knudson, Ltd., Washington, DC]).

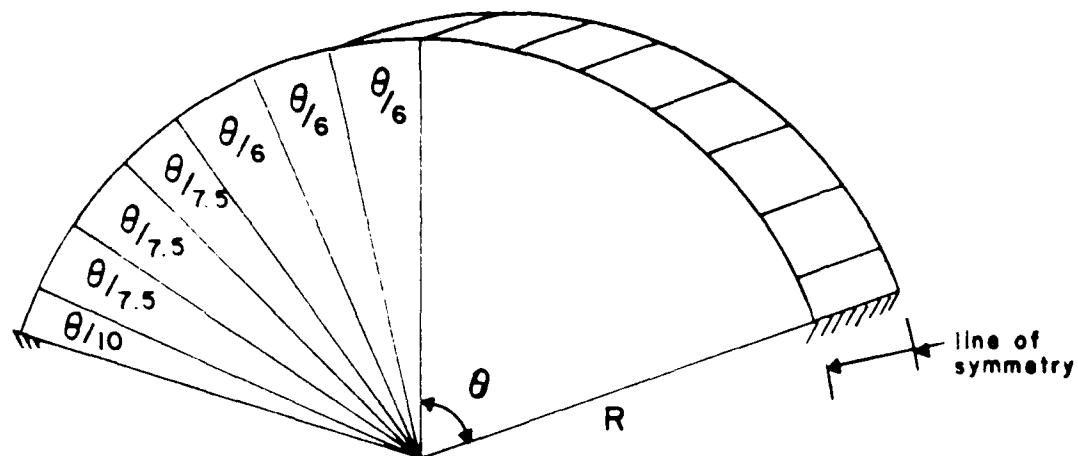


Figure 4. Finite element mesh used for the orthotropic model with 9-node Lagrangian elements.

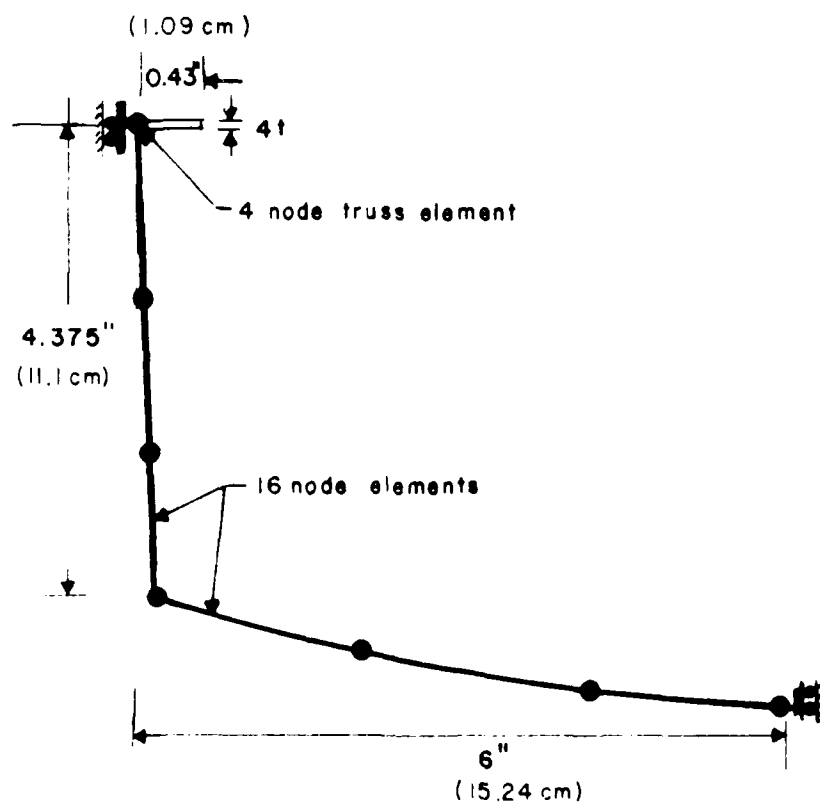


Figure 5. Section of the detailed model used with 16-node Lagrangian elements.

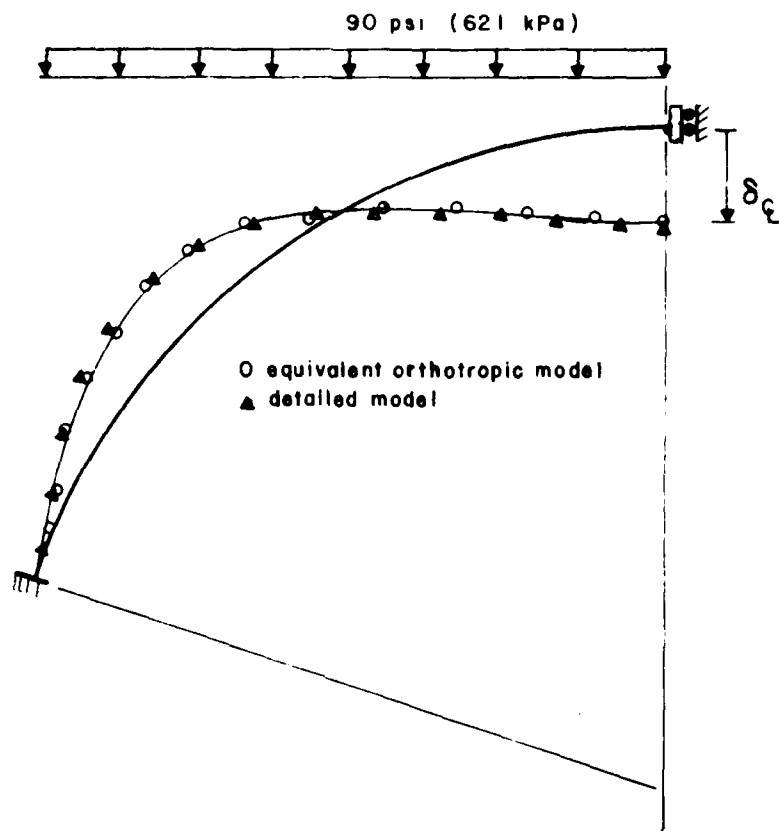


Figure 6. Deformation patterns of the 72 by 26 ft building obtained by the orthotropic and the detailed models.

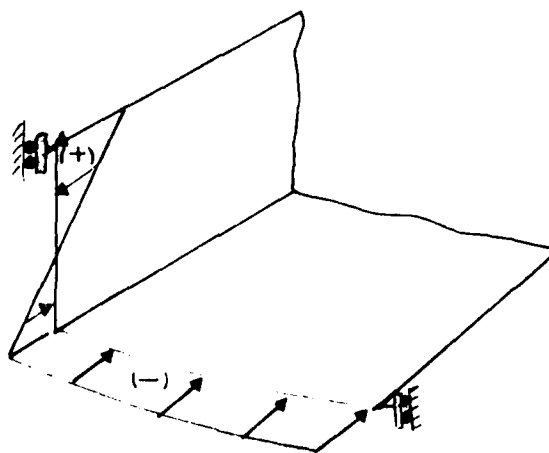


Figure 7. Typical stress distribution in the cross section at the base of the structure obtained by the detailed model.

4 OVERALL BUCKLING AND LOCALIZED NONLINEARITIES

The first phase of the present investigation consists of an analysis of the overall buckling behavior of the two structures under wind and snow loads using the orthotropic model. This model is good as long as localized nonlinearities (such as yielding or local buckling) are not present, or if present do not interfere with the geometry and stiffness of the profile. Therefore, local buckling and material nonlinearities are not considered in this analysis. The orthotropic model is much more economical (has fewer degrees of freedom) than the detailed one; thus, it was preferred for this phase, when it was not known how important localized nonlinear effects would be. However, ignoring these effects at this phase is not only a matter of economy. Better insight into the overall buckling behavior of the structure is possible when it is isolated from localized nonlinear effects. But even without localized nonlinearities, the orthotropic model is still an approximation to the real structure, since shell-type behavior within the panels is not taken into consideration.

However, once this analysis for large deformations is completed for a particular load, the results are examined to see what role localized effects might play. It is therefore determined whether overall buckling or local factors are the dominant causes of collapse of these shell structures.

Large Building

Balanced Snow Load

Figure 8 shows the nonlinear behavior (load versus deflection) of the large building, obtained under balanced snow loading, and expressed with respect to the reference snow load $p_r = 90$ psf. This corresponds to a ground snow load of 100 psf. The snow load was increased to 180 psf, but buckling was still not reached, and the analysis was not continued beyond that point.

When localized nonlinear effects are neglected and the base of the structure is assumed to remain fixed, a symmetric mode of buckling is expected.¹⁹ However, the corresponding buckling load is unrealistically high. Actually, very high stress resultants are built up at rather low load levels, indicating that localized nonlinear effects (local buckling and/or yielding) should be expected to occur well before a load of 180 psf is reached. Yielding (assuming a yield stress of 50 ksi) is reached at the ridge (seam), at the base sections of the structure at a load of $0.63 p_r$. A hinged base is therefore a more realistic assumption for the nonlinear analysis of this case when localized nonlinearities, other than the initial assumption of a hinged base, are not included in the analysis.

According to the expressions given by Timoshenko and Gere, buckling of this type of structure under uniform pressure, with the base fixed, will occur at a load of 172 psf. If one assumes a hinged base, then the buckling load under uniform pressure (antisymmetric mode) drops dramatically to 72 psf. Figure 9, showing the load versus deflection curve, confirms this expected behavior, indicating that the buckling load for the antisymmetric mode under balanced snow load with the base assumed hinged, drops down to about 73 psf.

¹⁹S. D. Timoshenko and J. M. Gere, *Theory of Elastic Stability*, 2nd ed. (McGraw-Hill, NY, 1961).

Unbalanced Snow Load

Figure 10 presents the nonlinear behavior (load versus deflection) of the large building under unbalanced snow loading. One can see that the structure has not reached the limit point up to a load of 2.2 times the reference snow load of 100 psf ground snow load. The corresponding midspan deflection at the load of $2.2 p_r$ is 70 in. The stress resultants and moments developed in the structural system indicate that localized nonlinear effects are certainly expected at much lower load levels. For example, the top fibers of the corrugated profile at the base region of the nonloaded part of the structure reached yield stress (assumed to be 50 ksi) at a load of only $0.4 p_r$.

Wind Load

As can be seen from Figure 11, the wind loading did not introduce any significant nonlinear behavior in the structure up to 2.5 times the reference wind load of 90 mph. The large tensile wind load acting on the central and leeward sections of the building appears to stiffen the structure against possible overall buckling. In addition, the moments developed in the structure are not as significant as with snow load. Since the stress resultants developed in the structural system are relatively low, plasticity effects are not expected to be a problem.

Even for the large structure, the wind loading analysis indicated that overall buckling is not expected. Thus, given that the stiffness of a cylindrical shell increases with the decrease of the radius, using the orthotropic model for smaller structures would not result in any additional useful information. That is, this type of structure is considered safe against wind loading as far as overall buckling and material nonlinearities are concerned. The effects of local buckling under wind loading are discussed later.

Intermediate Building

Balanced Snow Load

Figure 12 presents the nonlinear behavior (load versus deflection) of the intermediate cylindrical shell structure under balanced snow loading. The base is assumed to be fixed. The deflections are much smaller than the corresponding deflections of the large building, and for loads up to 270 psf the limit load is not reached. The analysis was not continued beyond that point, since localized nonlinearities are expected to occur at much lower load levels. At the base of the structure, yielding at the extreme fibers of the corrugated profile (seam) is expected to be reached at a load of only $1.4 p_r$. As in the case of the large building, the more realistic assumption of a hinged base was investigated.

Antisymmetric buckling under the balanced snow load is presented in the load versus deflection curve in Figure 13. It shows a significant drop in the buckling load, but that load is still much higher than the corresponding buckling load of the large building. The limit load is reached at a load of 2.8 times the reference load, indicating that localized nonlinearities are expected to play a deterministic role in the buckling behavior of this structure under a balanced snow load.

Unbalanced Snow Load

The nonlinear behavior of the intermediate building under unbalanced snow loading is shown in the load versus deflection curve of Figure 14. The limit load was not reached

up to a load of 3.1 times the reference unbalanced snow load. The seam of the corrugated profile yields at the base of the nonloaded half of the shell at the reference load. As expected, this is a significantly higher load than the corresponding load of the large building.

Localized Nonlinearities

The overall buckling analysis of the large and intermediate buildings reveals that, in general, this type of structure will not collapse in an overall buckling mode. Instead, localized failures will cause collapse. This is because high, local, circumferential stress resultants develop at rather low load levels. It is important to note that the flexural term of Equation 4 is the main source of these stresses in the corrugated profile. High moments are developed along the circumference of the shell as a result of the high flexural rigidity of the corrugated sheets.

As expected, the large building shows a tendency to develop much higher circumferential bending moments than the intermediate building, for the same loading level. This means that the larger the building the more sensitive it is to overall buckling and, especially, to localized nonlinear effects. Since the large building is the largest currently constructed, one should expect that localized nonlinearities also govern the ultimate load capacity of any size building of this type.

In particular, the results of the overall buckling analysis provide a preliminary estimate of the expected importance of the localized nonlinearities, as summarized below.

Wind Load

The overall buckling analysis showed that this type of structure will not collapse under wind loading. The significant moments developed however, might result in local buckling (especially in the case of the large building) and, eventually, in the formation of some type of a collapse mechanism. Material nonlinearities are not expected to arise in this case.

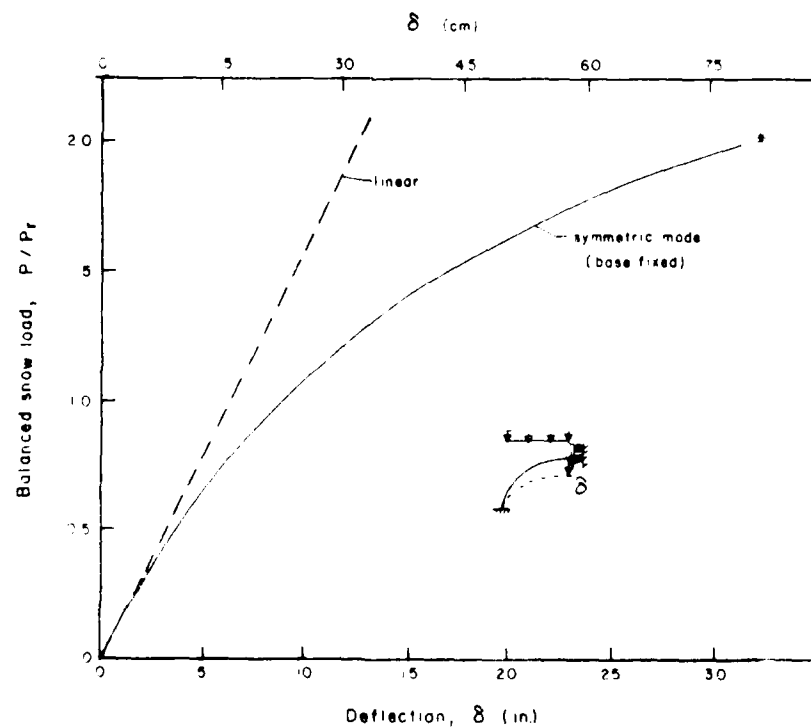
Balanced Snow Load—Large Building

In the case of balanced snow loading, the buckling load of the large building for the antisymmetric mode (hinged base assumed) is much lower than that of the intermediate building. However, overall buckling in an antisymmetric mode is possible only if hinges are formed at the base of the building. Such hinges could be caused by local buckling or yielding at a load below the corresponding limit load. This limit load was obtained earlier by assuming the base was hinged but ignoring other nonlinearities (see, for example, Figure 9). The overall buckling analysis shows that yielding at the fixed base is reached at a lower load than the corresponding limit load. The structure will then collapse at the limit load (antisymmetric mode) or, at a lower load, if a collapse mechanism is created due to local buckling. This last case can occur if at least two more hinges are formed in regions other than the base regions of the structure. It is therefore certain that overall buckling will not govern the collapse of a shell-type building of any size. Thus, the limit load corresponding to the antisymmetric (hinged base) mode of the large building is an upper bound on the balanced snow load that will cause collapse. To determine the actual balanced snow load governing the collapse of the large building, localized nonlinear effects must be considered.

*Unbalanced Snow Load—Large Building;
All Snow Loading—Intermediate Building*

The buckling behavior of the large building under unbalanced snow loading and of smaller buildings under all snow loading cases seems to depend strongly on the type of nonlinearities which may develop and the possible interaction of these local effects with the overall nonlinear behavior of the structure. Since in all these cases no significant nonlinear behavior was observed even under high loads, it is more probable that the governing collapse load will be related only to the development of a collapse mechanism caused by localized nonlinear effects.

It is evident, then, that local buckling and, in some cases, yielding are major considerations in the determination of the ultimate loads of these structures. However, one cannot predict the corresponding collapse loads of these cases based on the information obtained by the preliminary nonlinear analysis, which used the equivalent orthotropic model. It is therefore necessary to investigate in more detail the probable bending behavior of the typical corrugated panel, since bending is the basic mechanism by which localized nonlinearities develop. This investigation will determine the specific localized nonlinearities which prevail when high circumferential bending stresses develop along the corrugated profile. The development of such localized nonlinearities can be examined if material and geometric nonlinearities are considered in the analysis by using appropriate refined meshes. In addition, approximate analytical methods or experiments may be used.



*Analysis not continued beyond this point.

Figure 8. Nonlinear behavior of the large building under balanced snow loading, assuming symmetric mode with fixed base ($p_r = 100$ psf ground snow load).

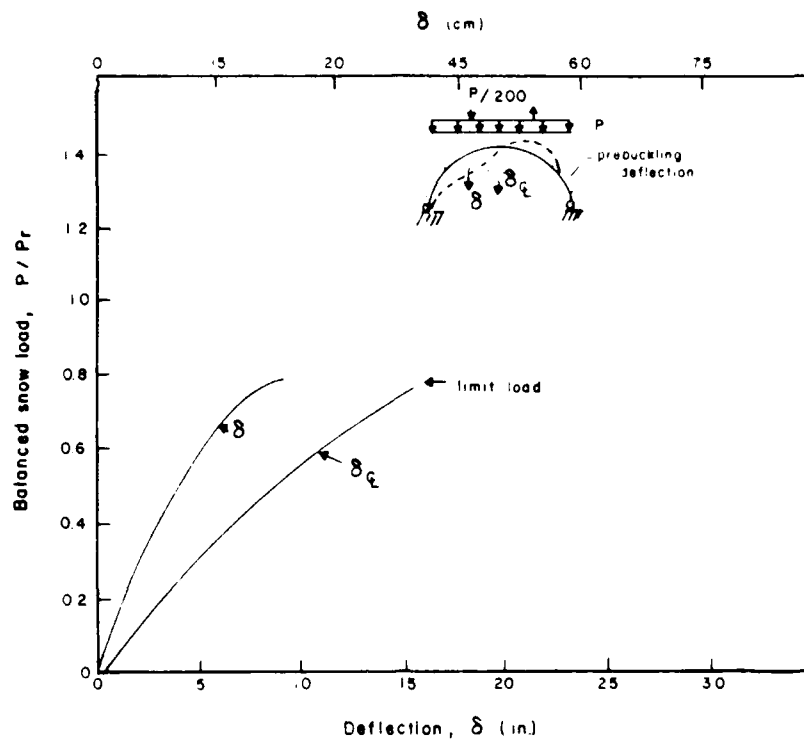
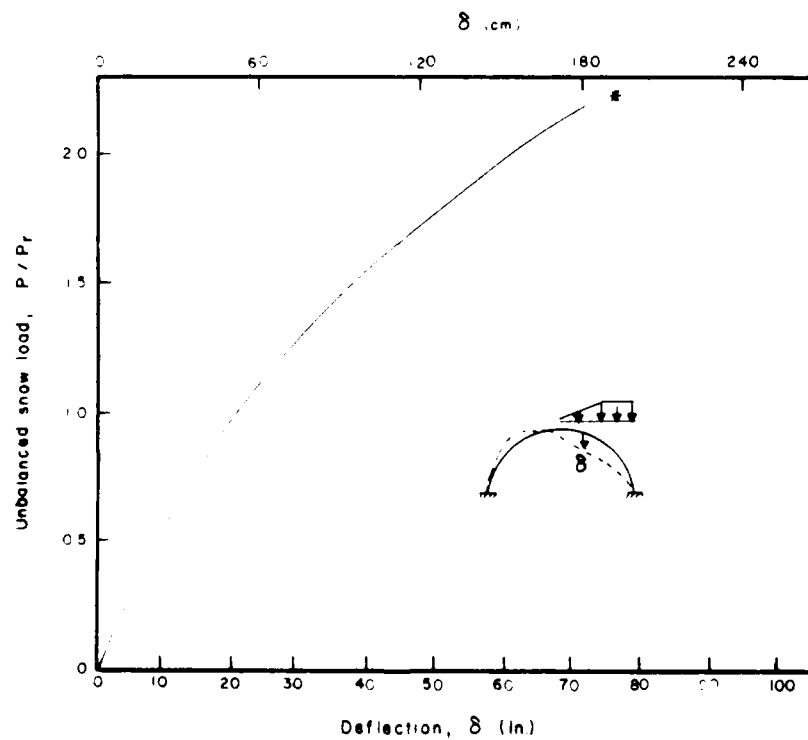
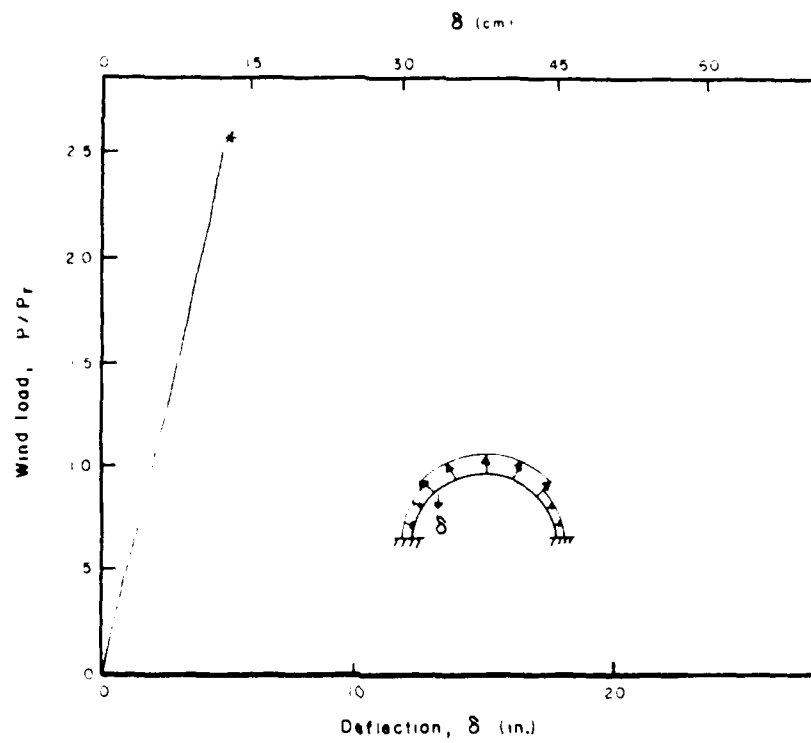


Figure 9. Nonlinear behavior of the large building under balanced snow loading, assuming antisymmetric mode with hinged base ($p_r = 100$ psf ground snow load).



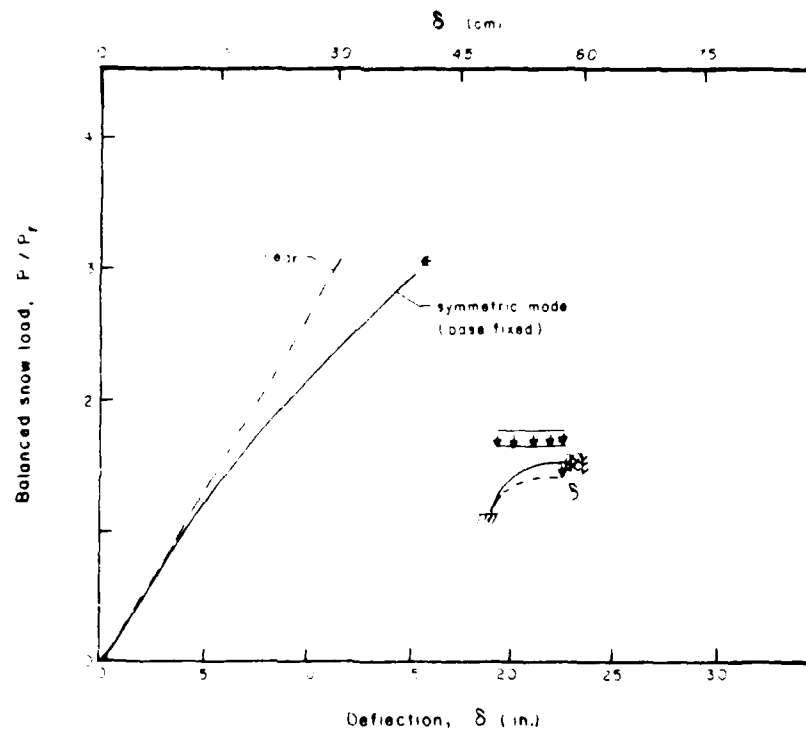
*Analysis not continued beyond this point.

Figure 10. Nonlinear behavior of the large building under unbalanced snow loading ($p_r = 100$ psf ground snow load).



*Analysis not continued beyond this point.

Figure 11. Nonlinear behavior of the large building under wind loading (reference velocity 90 mph).



*Analysis not continued beyond this point.

Figure 12. Nonlinear behavior of the intermediate building under balanced snow loading, assuming symmetric mode with fixed base ($p_r = 100$ psf ground snow load).

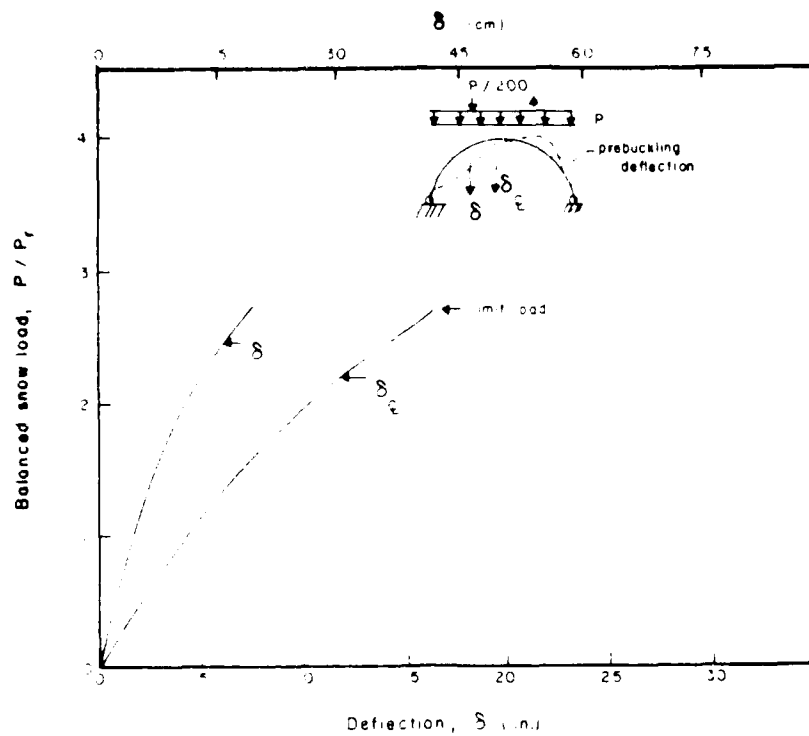
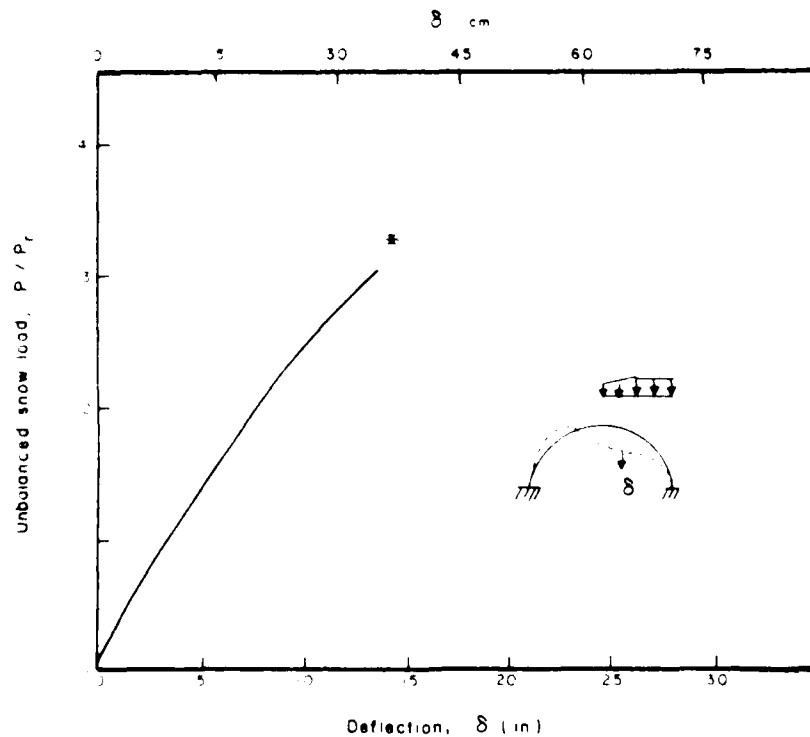


Figure 13. Nonlinear behavior of the intermediate building under balanced snow loading, assuming antisymmetric mode with hinged base ($p_r = 100$ psf ground snow load).



*Analysis not continued beyond this point.

Figure 14. Nonlinear behavior of the intermediate building under unbalanced snow loading ($p_r = 100$ psf ground snow load).

5 CRITICAL MOMENTS AND LOCAL BUCKLING

This chapter deals with the determination of the critical moments, which are defined as those moments which cause local buckling or cause a hinge to form, due to compression in the seam or flanges of the section. The critical moments of a typical panel of the corrugated shell and a typical straight panel were determined by analyzing the panels as simple beam structures under concentrated loads (first as cantilever, then as simply supported structures). The two finite element models were used in these analyses. Full-scale tests performed on the same panel-beam structures provided additional information which was used in determining the bounds of the critical moments.

The development of a collapse mechanism through the formation of hinges is examined with the analysis and full-scale tests of an arch section of the intermediate building, loaded under a line load at midspan. The critical moments determined with the panel-beam structures are confirmed, and, in addition, the effect of initial imperfections is assessed.

Critical Moments

In the panel cross section, the axial stresses which developed are the moment fiber stresses due to the moment field. These stresses are expected to result in the same type of localized nonlinear effects as in the case of the full arch shell structure. To determine the critical moments at the fixed base of the arch, the panel-beam was analyzed and tested as a cantilever beam; for the critical moments away from the base, it was analyzed and tested as a simply supported beam. Since compressive stress can develop either in the top fibers (seam) or the lower fibers (flange) of the typical panel (Figure 2), two cases were analyzed: one with the load applied upwards (negative moment) and one with the load applied downward (positive moment).

This study is complicated somewhat by the fact that the cross sections also have minor corrugations in addition to the seams (Figure 3). Initially, no attempt was made in the numerical analysis to model these minor corrugations with orthotropic properties, because they are nonuniform along the cross section of the panel. Their effect was to be evaluated by comparing the numerical results with the test results. However, they had to be approximated later in the nonlinear analysis, because of problems encountered in the course of the full-scale tests. In the case of the straight panel-beams, though, the numerical analysis results can be compared directly with those of the full-scale tests because straight panels have no minor corrugations. Details of the full-scale test arrangements, loading procedures, and measurements will be discussed in a separate technical report.

Cantilever Panel-Beam

A special case for the critical moment is the one which causes local buckling at the region of a fixed boundary (base of the arch structure). Because of the fixed conditions one would expect higher critical moments there than in regions away from the base. The structure used to test this was a section of the intermediate building, simulating a cantilever, curved panel-beam under concentrated load applied at the ridge of the free end. A series of full-scale tests was performed with this structure. The critical moments obtained from those tests are considered to be upper bounds for the critical moments that will cause local buckling at the fixed base of the real arch structure.

These experimental upper bounds are 3400 lb-in./in. for the critical positive moment (from the most reliable test of the series) and 2400 lb-in./in. for the critical negative moment (the minimum critical negative moment obtained from the tests).

Because only upper bounds to the critical moments were obtained by the cantilever beam tests, numerical analyses were also performed on a model of the same curved cantilever beam using eight 16-node Lagrangian elements.²⁰ Two elements were used in the longitudinal direction (double the detailed model across the panel shown in Figure 4). Symmetry was imposed along the center line between adjacent flanges and adjacent ridges for the critical negative and positive moments, respectively. This model does not include the effects of the minor corrugations. Those effects are examined later. In addition, because of numerical problems encountered when beam elements were used to simulate the seam (due to the resulting extreme thickness ratio), truss elements were used instead to model the seam section. This introduced some limitations to the validity of the model. Because of this approximation, the critical positive moment (compression at seam) of 2200 lb-in./in. obtained at the fixed end of the beam is quite low. This critical moment corresponds to buckling of the web plates rather than buckling of the seam "column-beam" supported by the web. The effect of the minor corrugations present in the web plates, however, would be to promote a "column-beam" type of buckling of the seam. Therefore, the lower bound to the critical positive moment at the fixed end will be assumed to be equal to the critical positive moment away from the base, as determined numerically in the next sections.

Because of the unrealistic modeling of the cantilever beam with respect to the positive critical moment, the curved cantilever beam was analyzed again, with a different mesh, using forty-eight 9-node Lagrangian shell elements²¹ while six beam elements were used to simulate the seam. Only geometric nonlinearities were considered because of a material nonlinearity option was not available for this element in FINITE. This did not introduce any major problems since it is easy to determine when yielding is reached at the ridge of the panel from the stress resultants obtained from the nonlinear analysis (large deformations). In this case, material failure is expected to initiate local buckling of the section. Local buckling was not obtained in this case, probably because a "perfect" section was modeled. Yielding was reached at the ridge level at a moment of 3500 lb-in./in. If minor corrugations are taken into consideration, this limit moment would be lower (discussed later). Therefore, a realistic upper bound to the critical positive moment at the fixed base of the arch structure is $M_{cr}^+ = 3400$ lb-in./in.; the value obtained from the tests of the cantilever beam. Thus, the upper bound of the critical positive moment at the fixed base is confirmed.

However, the approximate modeling of the ridge section by truss elements is not expected to affect negative moment corresponding to local buckling of the flange. Thus the negative critical moment obtained with the 16-node elements model, 1200 lb-in./in., is considered a reasonable lower bound. Note, however, that the effect of the minor corrugations on this lower bound is not included in this numerical analysis of the curved panel-beam. (It is considered later.)

For a straight cantilever panel-beam, the critical positive and negative moments were found to be 1900 and 1000 lb-in./in., respectively. There were no minor corrugations to complicate the analysis in this case.

²⁰K. J. Bathe.

²¹L. A. Lopez.

The Simply Supported Panel-Beam

To study local buckling away from fixed boundaries, it was decided to model a simply supported "beam" under two "third point" concentrated loads. Figure 15 shows the typical panel. Conditions of symmetry were assumed along the longitudinal edges. The finite element model employed, using FINITE, consisted of 48 Lagrangian shell elements and six beam elements; the latter elements model the ridge of the panel. Two variations of this model were used: a straight beam and a curved beam, both simply supported.

Straight Beam, Simple Support

Figure 16 gives the test results obtained from a single straight panel-beam loaded downward (positive moment). The letter "b" in the figure designates that lateral bracing was introduced at the ends of the beam to prevent warping. These results were "translated" to an equivalent span of 7 ft in order to make a direct comparison with the numerical analysis results. The same figure shows the results obtained by the nonlinear finite element analysis. The test and numerical analysis results agree well, as far as the general behavior is concerned. In addition, the level of stress in the panel cross section obtained numerically agrees with the test data (Figure 17), up to the point when plasticity effects become evident in the full-scale test results. The test results indicate that material failure initiates local buckling. Local buckling of the thin web and the seam of the panel is the actual, final mode of failure of the beam. This was verified by observation during the full-scale tests. Local buckling occurs when yielding is reached at the ridge, as the stiffness of the panel-beam structure decreases.

An initial imperfection in the panel cross section was introduced in the Finite element model by assuming nonsymmetry in the web. In addition to this geometric imperfection, a load imperfection was applied to introduce a nonsymmetric mode of buckling. (As is the usual practice, 1/1000 of the applied load was assumed to act laterally at the load point.) These two imperfections resulted in local buckling at a much lower load compared to the "perfect" beam structure. Figure 18 presents the configuration of the panel cross section before and after the local buckling. Note that the imperfection was assumed to be constant throughout the beam length. The straight panel structure is therefore sensitive to initial imperfections. (A sensitivity analysis was not performed at this point, because of cost and time limitations.) It must be emphasized that the real structure is at least nonsymmetric (not perfect with regard to the finite element model assumptions), due to the eccentric position of the seam with respect to the web center line. Initial imperfections are always expected in a real structure, but there is no predictable pattern to represent them.

To summarize, according to the numerical analysis, for an imperfect, straight beam, the critical positive moment is shown to be 1900 lb-in./in. (a value which, however, depends on the degree of imperfection). According to the test results, the critical positive moment is found to be 2600 lb-in./in.

Figure 19 presents the behavior of the straight panel under negative moment. In general the curves of the full-scale tests and the numerical analysis agree well. Both indicate a significant, shell-type behavior within the panel-beam structure. This is evident from the differential displacement observed between the center line and the line of symmetry of the panel. The full-scale tests indicate that in this case the mode of failure is not initiated by material failure (yielding at the ridge of the panel).

A major discrepancy is found in this case: the level of stress at the ridge in the full-scale tests is shown to be about half the corresponding level of stress found in the

numerical analysis. Comparing the level of stress between Figures 16 and 19, one concludes that the stresses calculated numerically are reasonable. At the same loading level, in the linear elastic region, they are about the same magnitude with opposite sign, as expected. Technical problems associated with the load application and the simulation of the boundary and support conditions may have contributed to the unexpected behavior of this series of tests.

An abrupt change in the displacement of the flange is observed in the numerical analysis curve obtained at $p/p_r = 1.5$ (Figure 19), but it is restricted to the elements in the region of the center line (midspan). This behavior indicates that local buckling might occur at that level of loading if a finer mesh was used to model this region. The model used, with six elements along half of the beam, eight elements along its width, and six beam elements, probably could not model local buckling displacements restricted to a very narrow area in the vicinity of the central line region. Note that according to the observations made in the full-scale tests, this area was only 2 to 3 in. wide. The mesh required to model such displacements would make the nonlinear analysis far too expensive.

Curved Beam, Simple Support

Figure 20 shows the results of the full-scale tests on a curved panel-beam loaded downward. As before, curves designated by "b" indicate lateral bracing imposed at the ends of the panel, whereas "u" indicates that no bracing was used in that particular test. As expected the panel-beams with no bracing failed at a lower load than the braced ones. In the braced beams the level of stress at the ridge at failure indicates that yielding initiated a combined mode of material and local buckling failure. In the unbraced beams, yielding had not been reached at the ridge when the beams failed due to local buckling. The fact that the braced beams did withstand higher loads than the unbraced ones shows that the local buckling of the ridge-web area is directly related to lateral buckling of the section as a whole.

There were some differences and inconsistencies in these full-scale tests that the critical load (and so the critical positive moment) obtained from these tests is, in general, about double the corresponding one for the straight panel-beam. Further, in comparing the stresses at the ridge obtained from the straight and the curved beam tests, it was found that the stress level at the ridge of the curved beam is lower than that of the straight beam for the same moment. This behavior is the opposite of the expected behavior. Another inconsistency is the stiffening effect observed in most of the curves of the full-scale tests (Figure 20). These unexpected results are related to problems associated with the simulation of the boundary and support conditions and with the load application.

In the analysis of the curved beam, as for the straight beam, a load imperfection (a horizontal force equal to 1/1000 of the applied vertical load) was introduced to initiate a nonsymmetric mode of buckling. In this case, however, no initial geometric imperfections were assumed. The numerical analysis results for the curved beam differ from the test results. The curved panel-beam seems to be stiffer than in the tests, probably because the analysis did not account for minor corrugations, which would have reduced the circumferential extensional and textural rigidity. The numerical analysis also indicates that local buckling governs the mode of failure of the structure at a rather low loading level. This load is comparable to the critical load obtained numerically in the case of the straight panel with initial imperfections.

To further investigate the effect of the minor corrugations present in the web and the flange of the panel, their equivalent orthotropic properties were calculated and introduced in the finite element model.

These properties were derived according to the method presented by Briassoulis.²² A triangular shape was assumed for the corrugations, and they were considered to be uniform across the width of the flange and the web. These assumptions constitute a simplifying approximation, but the objective was to confirm the tendency in the behavior rather than to obtain exact analytical results. The results obtained are shown in Figures 20 (the curve designated as orthotropic) and 21. As expected, the stress at the ridge level is higher compared to the curved beam without minor corrugations, for the same moment. In addition, the beam with the minor corrugations becomes softer.

Based on the numerical analysis results, it is clear that the critical positive moment can not be greater than the one corresponding to a load $\nu/p_r = 5$. At this loading level, the numerical analysis indicates that local buckling occurs in the isotropic beam (no minor corrugations considered). Also, at the same loading level, yielding is reached at the ridge of the panel when minor corrugations are included (approximated by equivalent orthotropic properties). The presence of the minor corrugations does not alter the positive critical moment in this case. Thus, it may be assumed that $M_{cr}^+ < 2300$ lb-in./in. This critical moment is within the range of the critical moments obtained with the full-scale tests of the straight beam (2600 lb-in./in., p 27) and the numerical analysis results for the straight, simply supported beam (1900 lb-in./in.; imperfect beam, p 27). This critical positive moment of 2300 lb-in./in. was also considered to be a reasonable lower bound for the critical positive moment at the fixed base (curved, simply-supported beam analysis). This is because the critical moment at the fixed base is expected, in general, to be higher than the one away from the fixed base and also to be rather insensitive to initial imperfections.

Figure 22 shows the test and numerical results of the curved beam under negative moment. In this case, the mode of failure is governed by local buckling of the flanges, which occurs at stresses less than the yielding stress at the ridge. The reduced extensional stiffness of the flanges due to the presence of the minor corrugations (Figure 21) is expected to have some effect on the critical load for local buckling (compare with the straight beam). The behavior of all curved beams tested with negative moment is consistent. This time the lateral bracing does not have any effect on the local buckling. This was expected since local buckling now occurs at the flanges, where lateral buckling does not exist. The displacement differentiation δ_1, δ_2 was found to be insignificant in the full-scale tests, while the analysis indicates significant shell-type behavior. In general, the full-scale tests indicate that the curved panel-beam is stiffer when the load is applied upwards, which seems to be inconsistent. This, along with the insignificant shell type behavior observed in this case, is attributed to similar problems as were encountered in the two previous sets of tests. A lower critical load than the ones indicated in Figure 22 is therefore quite possible (and should be expected).

The significant shell behavior observed with the nonlinear analysis is probably due to the fact that the finite element mesh used was not fine enough in the region of the center line to model local buckling. There, the localized, abrupt displacements, caused by local buckling, occur in very narrow region of the flange. This was also the case with the straight panel. It can be said that the numerical analysis did not succeed in obtaining local buckling in the flange of the panel.

²²D. Briassoulis, "Equivalent Orthotropic Properties of Corrugated Sheets."

Critical Negative Moments

At the Base

The critical negative moment of 1200 lb-in./in., obtained from the numerical analysis of the curved cantilever beam (p 30) did not include the effects of the minor corrugations. As it was shown before, the minor corrugations affect the negative moments through a decrease of the corresponding stress developed at the flange plate, by 75 percent. Then, applying the factor 1.33 to account for this effect, one obtains a lower bound to the critical negative moment at the fixed end of 1600 lb-in./in. An upper bound to the critical negative moment of 2400 lb-in./in. was obtained from the full-scale tests of the curved cantilever beam (p 26).

Away From the Base

The critical negative moments away from the base were not determined from either the numerical analysis or the testing of the simply supported section. However, because this type of buckling is restricted to a rather small region, the results obtained for the cantilever beam can be used. Assuming that local buckling in the case of the cantilever beam occurred within a distance of 10 in. from the fixed base, the corresponding critical negative moment can be estimated by multiplying the moment at the fixed end by 0.85. This factor corresponds to the moment at 8 in. from the base and is based on observations made during the tests. Using the upper and lower bounds determined for the fixed base, the corresponding bounds away from the fixed base are estimated to be $0.85 \text{ by } 1600 = 1300 \text{ lb-in./in.}$ (lower bound) and $0.85 \text{ by } 2400 = 2000 \text{ lb-in./in.}$ (upper bound).

Local Buckling Considerations

In the numerical analysis discussed above, two critical moments (positive, negative) were determined, corresponding to two distinct modes of local failure of the panel. Local failure occurs at the ridge-web section under positive moments and at the flange under negative moments. The mode of failure is local buckling in a field of positive moment. This happens before yielding is reached at the ridge. In a field of negative moment, local buckling occurs at the flanges, and it is not associated with material failure (e.g., yielding at the ridge). Therefore, in the actual arch structure, both modes should represent a local buckling type of failure, which, in the case of positive moment, will be coupled with lateral buckling. In this last case, lateral restraint was shown to increase the load capacity of the panel (full-scale tests).

The presence of minor corrugations across the flanges and the web of the curved panel was shown to have some important effects on the structural behavior of the panel. One such effect is the decrease in the stiffness of the structure, which resulted in larger deformations. Specifically, in a positive moment field higher stress is required to cause local-lateral buckling. Yielding may be reached at the ridge, initiating the mode of local buckling failure. This corresponds to about the same moment as that which resulted in local buckling of the ridge-web section in the case of a beam without minor corrugations (away from the fixed base). In a negative moment field the stress level at the flanges is reduced, for the same moment. This may be assumed to increase the critical negative moment by a factor of 1.33, compared with the case when no minor corrugations are present.

The critical moments corresponding to local failure, as determined above, are used in the following sections to determine whether hinges could form in the structure and to investigate for possible collapsing mechanisms. It must be clarified here that the hinge formed in the panel after a local buckling type of failure is not equivalent to what is known as "plastic hinge" in limit analysis of concrete and steel structures. The panel will not keep its initial configuration after local buckling occurs at the ridge-web section (positive moment). Figure 18 gives an idea of the type of local deformation of the panel cross section. Severe deformations of the panel cross section of the same type were observed at the regions where local buckling occurred during the full-scale tests (loading downward, Figure 15). Since the bending rigidity of the panel comes primarily from its geometric configuration, it is reasonable to assume that the moment capacity of the panel at the section where local buckling occurs drops practically to zero. Of course, the reduction of the moment capacity will be gradual after its initial drop and it will follow the gradual formation of the hinge as the tilted web will further bend out of plane tending to "sit" on the flange. In addition, the deformation of the panel cross section extends to some distance away from the section where local buckling occurred, damping out gradually (Figure 18a). Hence, the equivalent orthotropic properties, and especially the circumferential bending stiffness of the panel, are reduced nonuniformly in the region surrounding the "hinge."

On the other hand, in a region of negative moment field, the flanges cannot carry any stress at all in the section where they have buckled locally. Then, since the bending stiffness of the web-ridge section alone is negligible, the "hinge" formed in a negative moment field region is also assumed to carry a zero moment.

Approximate Analytical Formulas

Analytical expressions for buckling of plates under different boundary and loading conditions can be used to obtain some indication of the expected critical moments for the panel under investigation.

The analytical expression given by Timoshenko and Gere for a plate simply supported along its longitudinal sides and placed under a stress distribution similar to the one shown for the web plate in Figure 17, yielded a critical stress at the ridge of 26 ksi that corresponds to a critical positive moment of 1900 lb-in./in., which is low compared to the one obtained numerically (2300 lb-in./in. [p 29]). Of course, the web of the panel is not simply supported, and the final local buckling mode of the ridge-web section is a type of local-lateral buckling of the seam-web section. In fact, it was observed that in a local-lateral type of buckling, the seam behaves as a column-beam and the flange behaves as a fixed base for the web plate. Therefore, the approximation of a simply supported plate for the web should be used very carefully and only to obtain some rough indication (conservative in this case) of the critical positive moment expected to cause local buckling.

Timoshenko and Gere's analytical expression for a plate fixed at its two longitudinal sides and placed under compression can be assumed to model approximately the behavior of the flange of the panel in compression, under a negative moment field. The corresponding critical stress to produce buckling at the flange is 2.0 ksi. The length of the region over which local buckling occurs in this case is rather short. This is in agreement with the observations made during the tests. The critical stress of 2.0 ksi at the flange corresponds to a stress at the ridge level of 6.3 ksi and to a load of 540 lb/panel, or $p/p_c = 1.4$. This is in the range of the loading level at which the abrupt change in the displacement of the flange of the straight beam (loaded upwards) was

observed (Figure 19). The analytical expressions for local buckling of a plate fixed along its two longitudinal sides, simulating the flange of the curved panel, yield a critical moment of 720 lb-in./in. (due to higher flexural rigidity of the curved panel). The corresponding local buckling develops in a rather short length of the flange, again verified by observations during the tests. In conclusion, the approximate analytical formulas for the determination of the critical negative moment yield conservative results. However, they should be used carefully, and then only to obtain a rough indication of the expected critical moments.

Arch Structure Under a Line Load

Numerical analysis was carried out for the intermediate sized arch under a line load located at midspan. This was done in order to compare results with those of the full-scale testing under similar conditions. The numerical analysis was carried out with the same orthotropic model used to analyze the structure under snow and wind loading, as discussed in earlier sections.

Figure 23 presents the numerical analysis results. In its initial condition, the arch is analyzed with a fixed base. For a critical positive moment of 2300 lb-in./in. ($p/p_r = 29$) the first hinge is expected to form at midspan, at a loading level of $p/p_r = 6.5$. When this hinge is formed, a moment redistribution takes place within the structure. The analysis of the arch with its base fixed and with a hinge introduced at its top yielded the second curve in Figure 23. The structure is much softer now, and a second hinge is expected to form under the same critical negative moment. This moment however, corresponds to a lower loading level than for the formation of the first hinge. Figure 24 shows the moment distributions in half the arch, before and after the formation of the first hinge. After the formation of the first hinge, the negative critical moment is reached at the quarter point of the arch at nearly half the loading level at which the first hinge was formed. Assuming that the load remains constant, the formation of the first hinge means total collapse of the structure, causing a simultaneous formation of hinges at the quarter points (see Figure 23).

Critical loads for the formation of the first and second hinges as measured in the full-scale tests are shown in Figure 23. The deflection of the structure measured during the tests was about three times as large as that obtained numerically. This is due to the presence of the minor corrugations and the resulting reduction in circumferential extensional rigidity of the real structure. Note that the same behavior was observed during the beam tests (Figure 20), and it was also confirmed numerically with the introduction of equivalent orthotropy in the flanges and web of the panel (Figure 20).

The critical positive moment away from the fixed base has been established numerically as 2300 lb-in./in. In the full-scale tests, stress at the ridge at buckling was measured to be in the vicinity of 30 ksi. The numerical analysis curves of Figure 20 give a corresponding positive moment in the range of 1200 to 1800 lb-in./in., depending on the exact orthotropy introduced by the minor corrugations. The same level of moment is shown to correspond to the arch tests shown by the curve of Figure 22. Hence the critical positive moment of 2300 lb-in./in. obtained numerically is confirmed to be a realistic upper bound (when initial imperfections are discounted). It is also confirmed that the critical positive moments established in the beam tests are too high.

The critical positive moments obtained in the full-scale tests of the arch were found to be lower than the corresponding moments obtained numerically, for several reasons. Symmetry conditions along the edges of the arch in the tests could be modeled

only at discrete points. Local buckling did not occur simultaneously in all four ridges of the cross section (four panel arch), indicating some nonuniformity of the system. This reflects the effect of the initial imperfections present in the shell and is in accordance with the numerical analysis results of the perfect and imperfect straight beam (Figure 16). Because the degree and pattern of potential initial imperfections in a real structure cannot be predicted, the minimum positive moment corresponding to the formation of the first hinge, 1200 lb-in./in. (Figure 23), can be considered as an approximate lower bound on the critical positive moment, to account for initial imperfections. This however, will not account for severe distortions of the panel sections.

For the critical negative moments, the results of the full-scale tests correspond well with the results of the numerical analysis. Earlier, the lower bound to the critical negative moment for the panel section away from the fixed base was determined numerically as 1300 lb-in./in. In the full-scale tests of the arch, the critical negative moment resulted in the formation of the second hinge at a quarter point of the arch. Based on the moment distribution obtained numerically for an arch with a hinge at the top, the critical negative moment developed in the tests is estimated to be in the range of 1300 to 2000 lb-in./in. The critical stress at the extreme fibers (ridge) was found to be an average of 35 ksi in the region where the second hinge was formed. This corresponds to a negative moment of 2000 lb-in./in. (Figure 22). By taking into account the effect of minor corrugations on the stress distribution within the curved panel (Figure 21), the corresponding stress is 0.75 by 35 ksi and the corresponding moment from Figure 22 is 1700 lb-in./in. This moment is higher than the lower bound of 1300 lb-in./in., but close to the upper bound of 2000 lb-in./in. determined previously.

It must be emphasized here, that from Figure 23 it is not possible to determine exactly the critical negative moment corresponding to the formation of the second hinge during the tests. This is because the formation of the first hinge in the real structure also affects the adjacent region of the arch by reducing the flexural rigidity of the panels there. So, the moment distribution obtained by the analysis of the arch with a hinge introduced at its top is not the exact distribution presented by the real structure. It is shown however, to be a good approximation, adequately verifying the range of the critical negative moment.

According to the results obtained then, the lower bound of the critical negative moment of 1300 lb-in./in. (1600 lb-in./in. at the fixed end) established in earlier sections (p 30) is a conservative estimate of the moment which will cause the flange of the panel to buckle locally under a negative moment field. It will be shown however, that even using a higher lower limit of 1500 lb-in./in. (1700 lb-in./in. at the fixed base), which is closer to the results of the arch tests, will not make any appreciable difference to the ultimate loads obtained. Note also that the upper bounds to the critical negative moment are 2400 lb-in./in. at the fixed base and 2000 lb-in./in. away from the fixed base (both obtained from the cantilever beam tests).

In general, the results obtained by the full-scale tests verify the critical positive and negative moments established previously, as upper and lower bounds respectively. They also verify that hinges will form and that collapse mechanisms will cause the arch structure to fail under different loading patterns. In conclusion, local buckling establishes the ultimate loads for this type of structure through the formation of hinges.

Summary of Critical Moment Bounds

The investigation of the formation of collapse mechanisms in the arch structure is based on the bounds (limits) on the critical moments. These moments were established and verified in the previous sections. Summarizing, the following conditions are expected to be met for the formation of a hinge.

1. Positive moment fields

a. At fixed base

$$\frac{2300}{M^+} < \frac{p_{cr}}{p_r} < \frac{3400^*}{M^+}$$

b. Away from base

$$\frac{1200^{**}}{M^+} < \frac{p_{cr}}{p_r} < \frac{2300}{M^+}$$

2. Negative moment fields

a. At fixed base

$$\frac{1600}{M^-} < \frac{p_{cr}}{p_r} < \frac{2400^*}{M^-}$$

b. Away from base

$$\frac{1300}{M^-} < \frac{p_{cr}}{p_r} < \frac{2000}{M^-}$$

*Determined from full scale tests.

**This lower bound was obtained from full scale tests of the arch. It is conservative and includes the effects of regular initial imperfections but not the effects of excessive distortions.

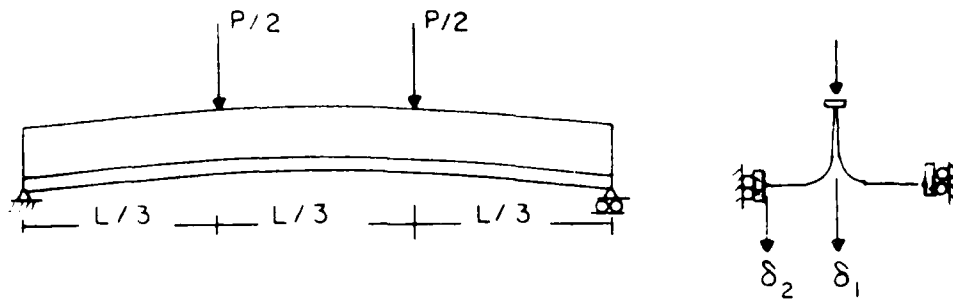


Figure 15. Typical simply supported panel-beam under two concentrated loads applied downward and upwards, tested in a series of full-scale tests, and analyzed numerically ($L = 7$ ft in analysis, $L = 6$ ft in tests).

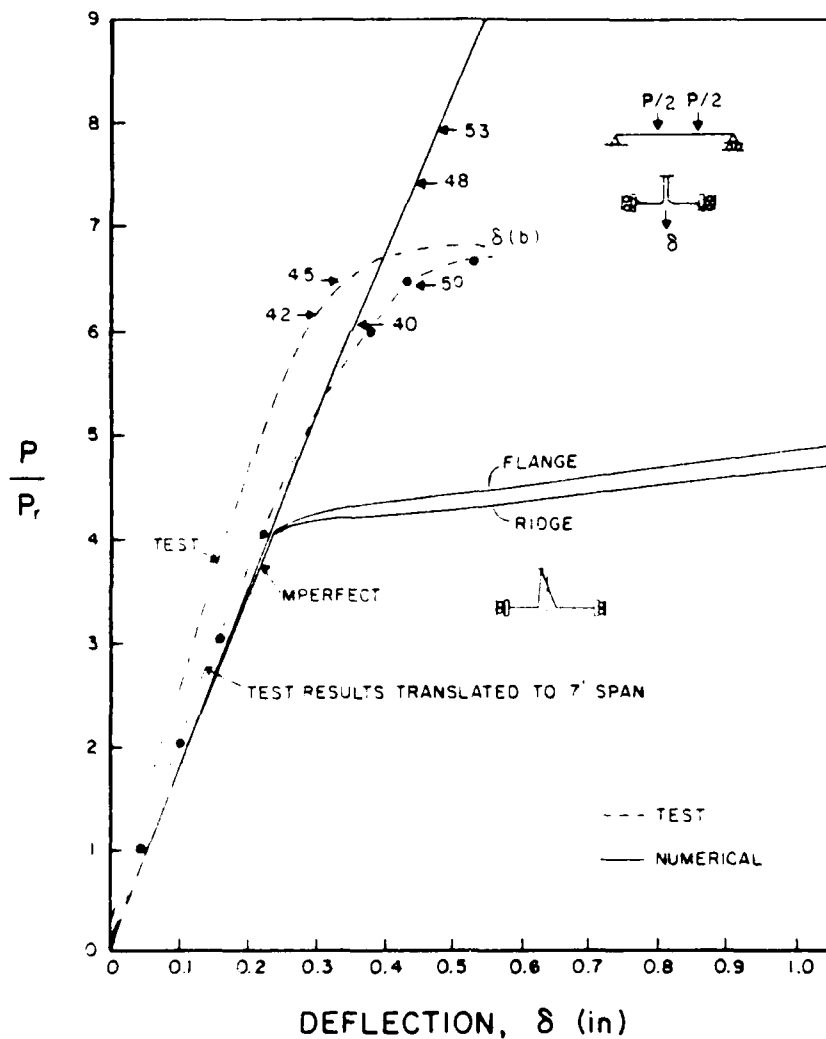


Figure 16. Nonlinear analysis and full-scale test results of a straight panel-beam, loaded downward (numbers on the curves indicate stress at the ridge in ksi).

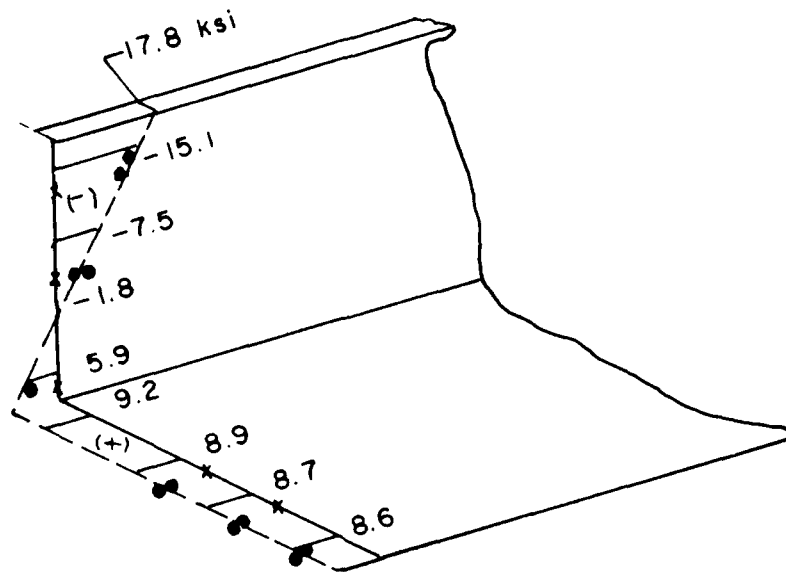


Figure 17. Stress distribution in a section of the straight panel according to the numerical analysis and the full-scale tests (solid circles indicate test results).

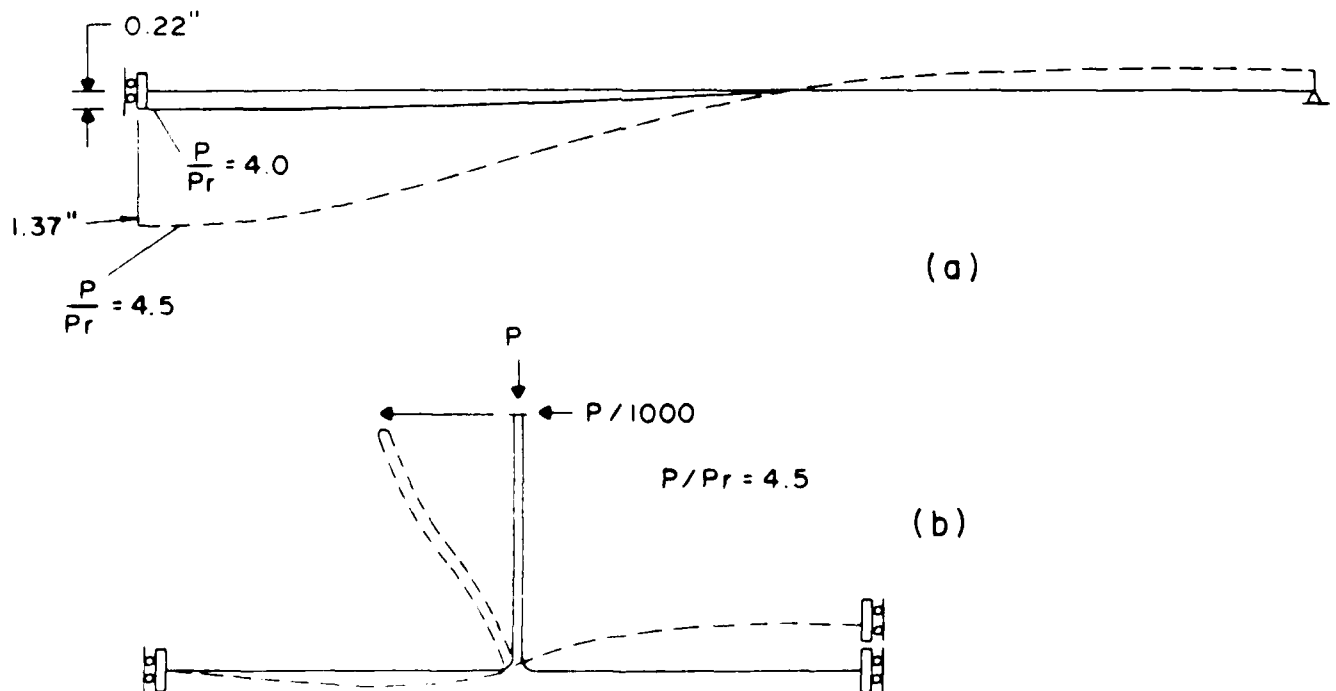


Figure 18. Lateral-local buckling of the straight beam in the presence of initial imperfections (numerical analysis): (a) lateral displacement of the beam; (b) deformation of the cross section.

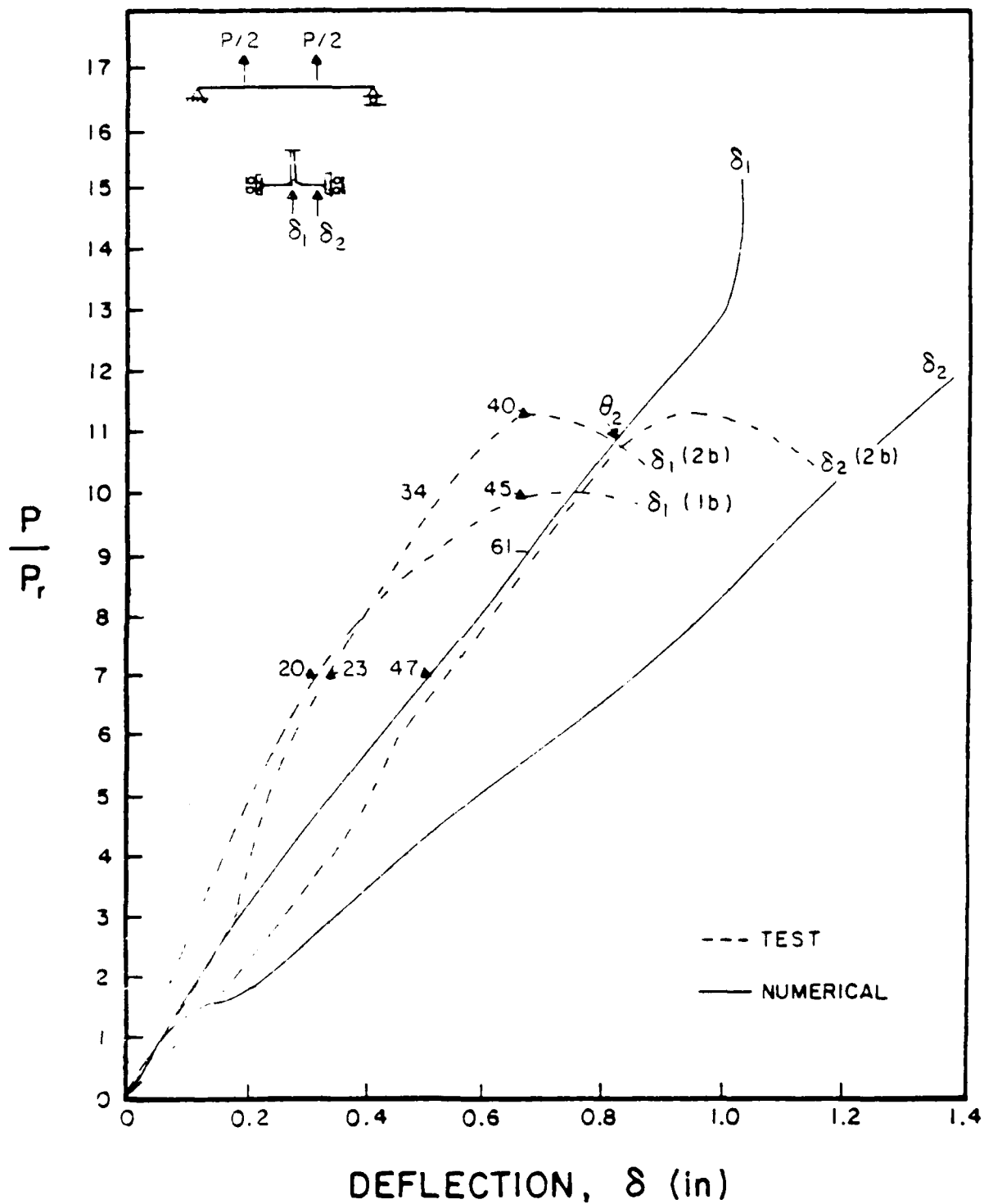
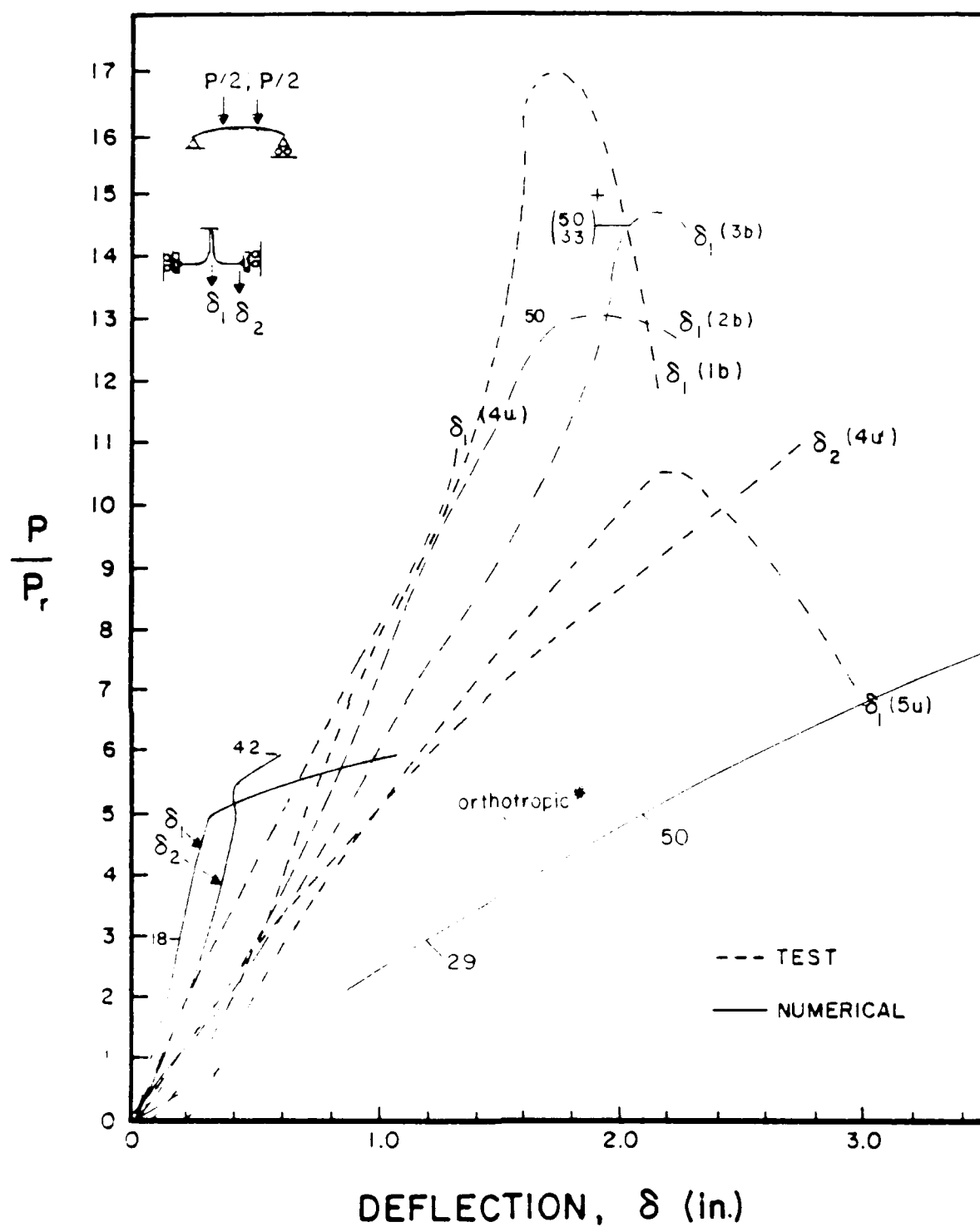


Figure 19. Nonlinear analysis and full-scale test results of a straight panel-beam, loaded upwards (numbers on the curves indicate stress at the ridge in ksi).



*Minor corrugations included.

Figure 20. Nonlinear analysis and full-scale test results of a curved panel-beam, loaded downward (numbers on the curves indicate stress at the ridge in ksi).

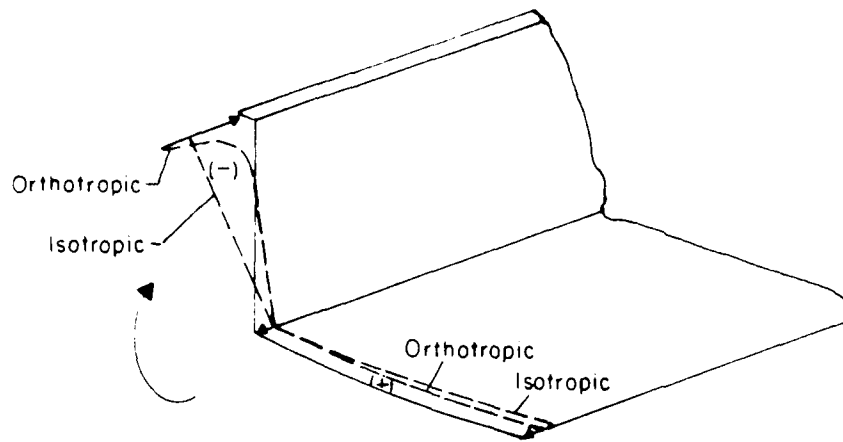
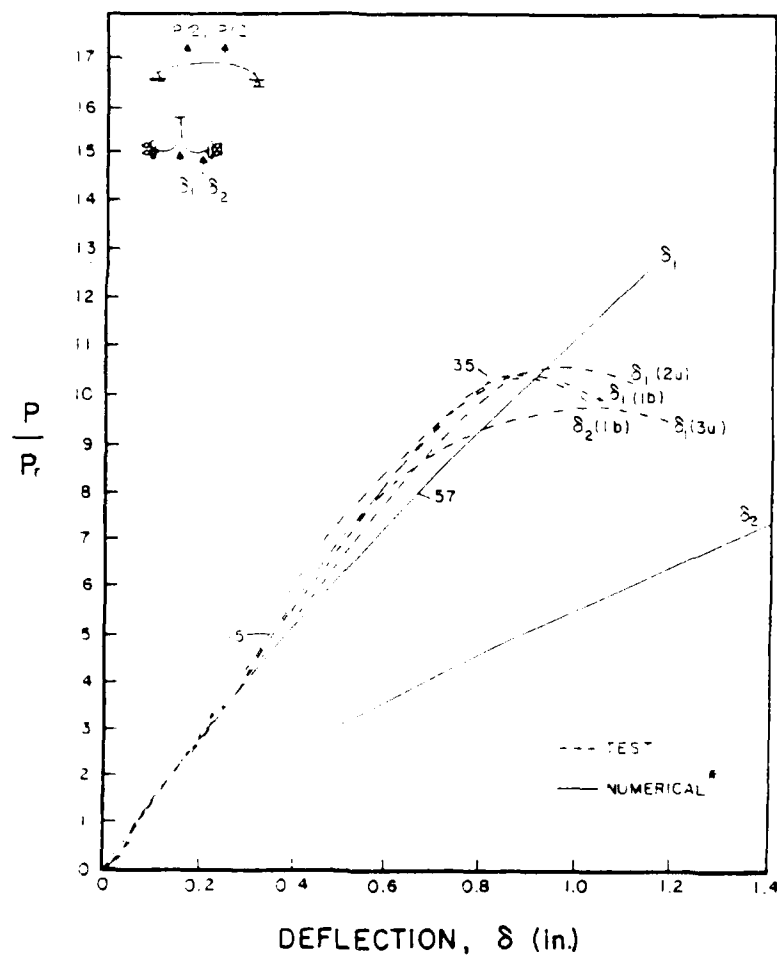
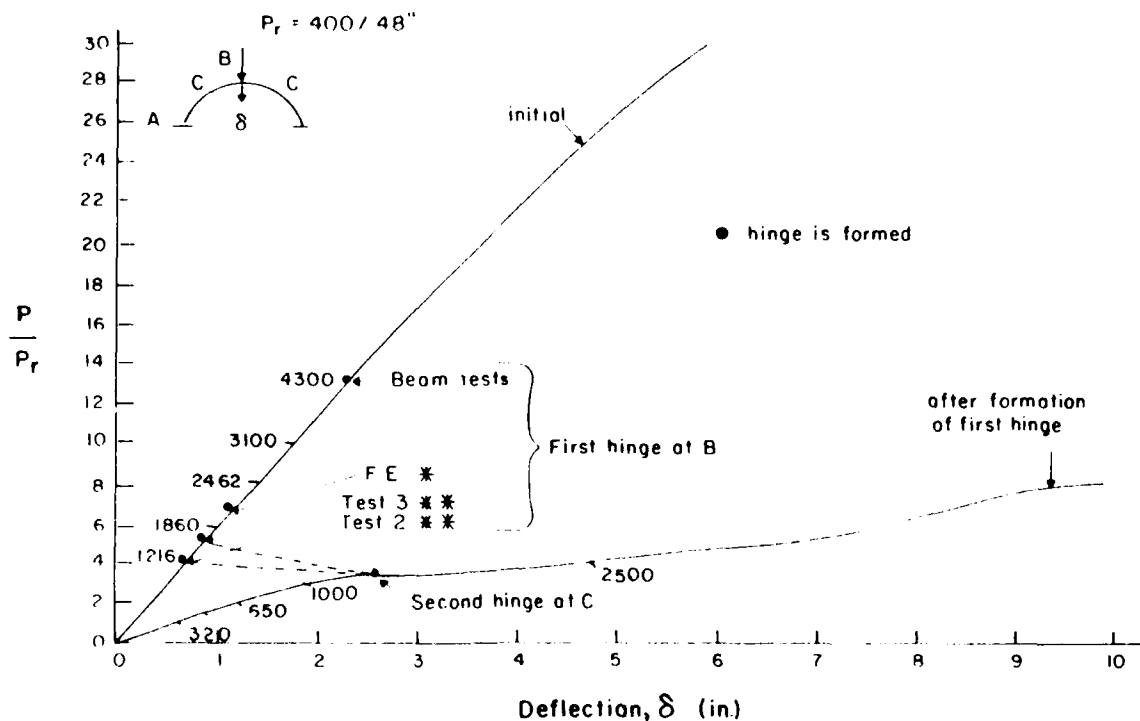


Figure 21. Stress distribution in the curved panel, with and without minor corrugations, modeled with isotropic and orthotropic shell elements, respectively.



*Minor corrugations neglected.

Figure 22. Nonlinear analysis and full-scale test results of a curved panel-beam, loaded upwards (numbers on the curves indicate stress at the ridge in ksi).



*Formation of first hinge according to critical positive moment obtained through finite element analysis of simply-supported panel-beam.

**Formation of first hinge according to full-scale tests.

Figure 23. Numerical analysis and full-scale test results of the arch structure under a line load. (On initial curve, numbers indicate moments at the top; on curve after formation of first hinge, numbers are moments at quarter points.)

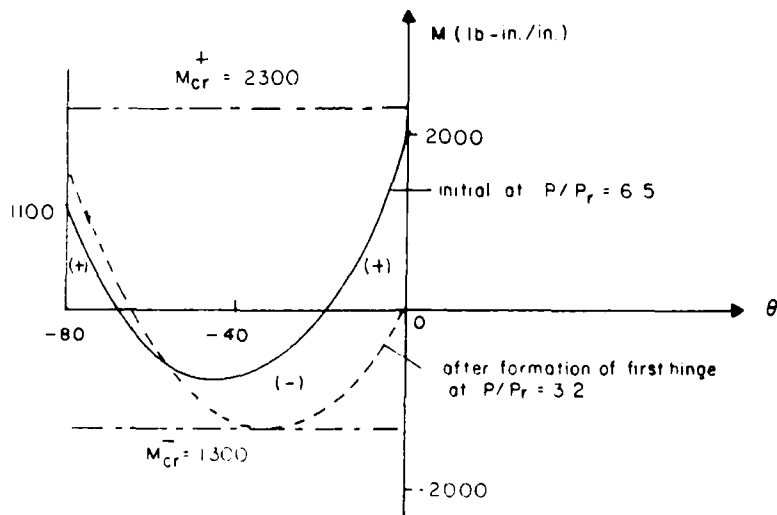


Figure 24. Moment distribution in half of the arch structure before and after the formation of the first hinge, corresponding to the critical positive and negative moment fields, respectively.

6 COLLAPSE MECHANISMS AND ULTIMATE LOADS

In this chapter the critical moments determined in Chapter 5 are used to determine ultimate wind and snow loading conditions based on loadings determined in Chapter 2. The method of analysis proceeds as follows. All critical loads corresponding to the extreme moments in the moment distribution under investigation are determined. The smallest of these loads defines the load at which the first hinge is expected to be formed. If other critical loads are close to the governing one(s), a simultaneous formation of all these hinges is expected due to the moment redistribution which follows the formation of the first hinge. Then, the governing critical loads define the bounds to the ultimate load of the structure under the loading being considered. It will be shown in the following sections that this is the case with the snow loading, balanced and unbalanced. Collapse under wind loading may follow a different pattern, however.

Balanced Snow Load—Intermediate Building

Figure 25 presents the moment distribution in the intermediate arch structure under the reference, balanced snow loading (100 psf ground snow load). To investigate where the first hinge will form and under what snow loading level, all extremes of the moment distribution are examined with respect to the bounds given in the previous section.

Starting from the base, where a positive moment of 3000 lb-in./in. develops, one expects the critical load to cause local buckling at that region to be bounded by $0.77 < p_{cr}/p_r < 1.13$. At the central region where the positive moment is 1500 lb-in./in., a hinge should be expected at a load of $0.80 < p_{cr}/p_r < 1.5$. For the formation of a hinge at the region of the maximum negative moment (approx. at quarter points), the critical load is also bounded by a minimum: $p_{cr}/p_r > 0.81$.

Therefore, taking the two lower bounds, one can predict that the lower limit of the ultimate balanced snow load is in the range of $p_{cr} > 77$ to 80 psf balanced snow load (ground load). This corresponds to a simultaneous formation of hinges at the base and at the quarter points (Figure 26a), and thus to instantaneous collapse of the structure.

In addition, taking the maximum limit for the formation of a hinge at the base, it can be said that the critical balanced snow load is $p_{cr} < 113$ psf balanced snow load (ground load). One can therefore estimate the ultimate balanced snow load to be 77 psf (conservatively), measured on the ground.

Note that the overall buckling of this structure, with hinges already formed at the base, was found in earlier sections to be 280 psf. This is far beyond the limits which govern the formation of collapsing mechanisms. Thus, it is confirmed that local buckling is the key factor in the determination of the ultimate loads of this type of structure.

Balanced Snow Load--Large Building

The large building presents a very similar moment distribution to the one exhibited by the intermediate building under balanced snow load, as expected (Figure 27). The relative magnitudes of the moments however, are larger for the large building and this results in much lower ultimate loads.

The critical load which will result in the formation of hinges at the base, where the positive moment is 7000 lb-in./in., is bounded by $0.33 < p_{cr}/p_r < 0.49$. Formation of a hinge at the center line of the arch requires a critical load bounded by $0.30 < p_{cr}/p_r < 0.58$. At the quarter points, the negative moment of 4300 lb-in./in. indicates a critical load which is $p_{cr}/p_r > 0.30$.

Then, one can define the lower limits of the ultimate load to be $p_{cr} > 30$ to 33 psf balanced snow load (ground load), and the upper limit of the ultimate load to be $p_{cr} < 49$ psf balanced snow load (ground load). The ultimate balanced snow load in this case can be assumed to be 30 psf (conservatively), measured on the ground.

Overall buckling of the large arch structure when hinges have already been formed at the base was found earlier to be 73 psf. This is still outside the limits corresponding to the formation of collapsing mechanisms. Therefore, a design consideration involving overall buckling and hinge formation at the base of the arch could be used, but only for very large buildings of the type under investigation.

Unbalanced Snow Load—Intermediate Building

Figure 28 presents the moment distribution within the intermediate arch structure, under a combination of wind and snow reference load (100 psf snow load on the ground), described as unbalanced snow loading.

At the fixed base where a maximum positive moment of 5500 lb-in./in. develops, the critical load to cause formation of a hinge is found to be bounded by $0.42 < p_{cr}/p_r < 0.62$. A hinge can also be formed in the second region of extremal positive moment, requiring that $0.35 < p_{cr}/p_r < 0.68$.

In the region where a maximum negative moment of 3000 lb-in./in. develops, away from the base, the critical load is bounded by $0.43 < p_{cr}/p_r < 0.66$. Similarly, with a negative moment of 3100 lb-in./in. at the base, the critical load which will cause local buckling is bounded by $0.51 < p_{cr}/p_r < 0.77$.

Hence, formation of hinges at the regions with the maximum negative moments and the fixed base with the positive moment could occur almost simultaneously, with any one of the three hinges being formed first to initiate the failure process (Figure 26b). Initial imperfections may cause the first hinge to form at the region of the second maximum positive moment. The bounds for the minimum ultimate unbalanced snow load which will cause a collapsing mechanism to form are $p_{cr} > 35$ to 42 psf unbalanced snow load (ground load), where the lower value accounts for initial imperfections and is considered to be conservative.

The ultimate unbalanced snow load is not expected to exceed the maximum critical load corresponding to the formation of a hinge at the fixed base (positive moment): $p_{cr} < 62$ psf unbalanced snow load (ground load). The design unbalanced snow load can then be estimated to be 35 psf (conservatively), measured on the ground.

Unbalanced Snow Load—Large Building

Figure 29 presents the moment distribution in the large building under unbalanced snow loading. The magnitudes of the moments developed in the large building are rather large compared to the ones of the intermediate building.

At the base of the windward side, a positive moment of 11,700 lb-in./in. results in the formation of a hinge at a critical load bounded by $0.17 < p_{cr}/p_r < 0.29$. In the region of the second extremal positive moment, the corresponding positive moment is bounded by $0.14 < p_{cr}/p_r < 0.26$.

At the base where a negative moment develops, a hinge is expected to be formed at a critical load bounded by $0.17 < p_{cr}/p_r < 0.34$. At about the same lower bound of the critical load (0.18), a hinge is expected to be formed in the region with the second extremal negative moment of 7700 lb-in./in.

Therefore, the lower limit for the ultimate unbalanced snow load is found to be $p_{cr} > 14$ to 17 psf unbalanced snow load (ground load), where the lower value accounts for initial imperfections and is considered conservative. In addition, the upper limit to the ultimate load, corresponding to the formation of the first hinge at the region with the second maximum positive moment, is $p_{cr} < 26$ psf unbalanced snow load (ground load). The ultimate unbalanced snow load, measured on the ground, is then assumed to be 14 psf, conservatively.

Wind Load

The wind loading case is analyzed first for the large building. In general, it is expected that this type of loading may become critical only for large buildings. Figure 30 presents the moment distribution in the large building under the wind reference loading (90 mph). Obviously, significant moments develop only in the windward side of the arch. The first hinge(s) are therefore expected to form in this region.

At the fixed base, for a negative moment of 3600 lb-in./in., the critical load is bounded by $0.44 < p_{cr}/p_r < 0.67$. In the region with the maximum positive moment, the critical wind load to result in the formation of a hinge bounded by $0.63 < p_{cr}/p_r < 1.20$. Therefore, the development of the first hinge is certainly expected at the fixed base of the windward side. However, the formation of a collapsing mechanism is not obvious in this case, because of the large difference between the critical moments corresponding to the formation of the first and second hinges. Thus one cannot assume a nearly simultaneous formation of more hinges after the formation of the first one, as was the case with the snow load. Therefore, collapse of the structure is not imminent after the formation of the first hinge, but a moment redistribution takes place, as shown in Figure 30. Note that again the effect of the first hinge on the flexural rigidity of the adjacent region of the panels is not taken into account in this analysis. So, the moment distribution obtained after the first hinge forms is approximate, but it is considered adequate for estimating the range of the ultimate wind load for the arch structure. The maximum positive moment after the formation of the first hinge becomes 4000 lb-in./in. and the corresponding critical load is bounded by $0.30 < p/p_{cr} < 0.58$. At the region with the maximum negative moment, the bounds are $0.65 < p/p_{cr} < 1.00$.

Collapse of the structure is not possible unless the second hinge is formed. It is therefore concluded that the ultimate wind load for the large building has a lower limit corresponding to the formation of the first hinge, and an upper limit corresponding to the formation of the second hinge, of $V_{cr} > 60$ to 68 mph wind velocity. In addition, the critical wind load (velocity) can not exceed the upper bound for the formation of the first hinge, which is $V_{cr} < 74$ mph. In this last case, collapse of the structure is imminent after the formation of the first hinge.

For the intermediate building, the ultimate wind load is found in the same way to be bounded by $V_{cr} > 87$ to 102 mph wind velocity. Again, the critical load can not exceed the upper bound for the formation of the first hinge, which is $V_{cr} < 110$ mph. Formation of the first hinge according to the upper bound of the critical wind load indicates imminent collapse of the structure.

The Effect of Higher Critical Negative Moments

Higher lower bounds for the critical negative moment fields were indicated by the arch tests, as discussed previously. However, the introduction of such limits (1500 and 1700 lb-in./in. instead of 1300 and 1600 lb-in./in.) resulted in minor changes. The values which changed were the lower limit of the ultimate balanced snow load of the large building and the lower limits of the ultimate wind loads for both buildings. The corresponding ultimate load for balanced snow loading was found to be 33 psf compared to 30 psf determined with the more conservative critical negative moments. The lower limit to the ultimate wind load is found now to correspond to a wind velocity of 62 mph compared to 60 mph determined previously. For the intermediate building, the lower limit to the ultimate wind load is found to correspond to a wind velocity of 90 mph, compared to 87 mph determined previously.

Hence, no major changes are observed from the two sets of values for the critical negative moment fields. Note also that the upper bounds to the critical moments established in the previous sections cannot be exceeded. These bounds however, may yield ultimate loads on the unsafe side.

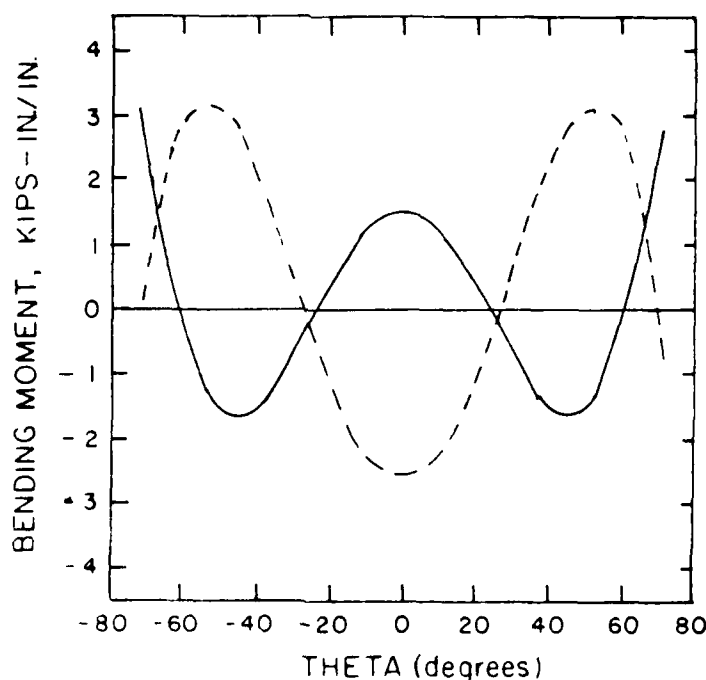


Figure 25. Moment distribution in the intermediate building under the reference balanced snow loading. (Dashed line corresponds to the moment distribution after the formation of hinges at the base.)

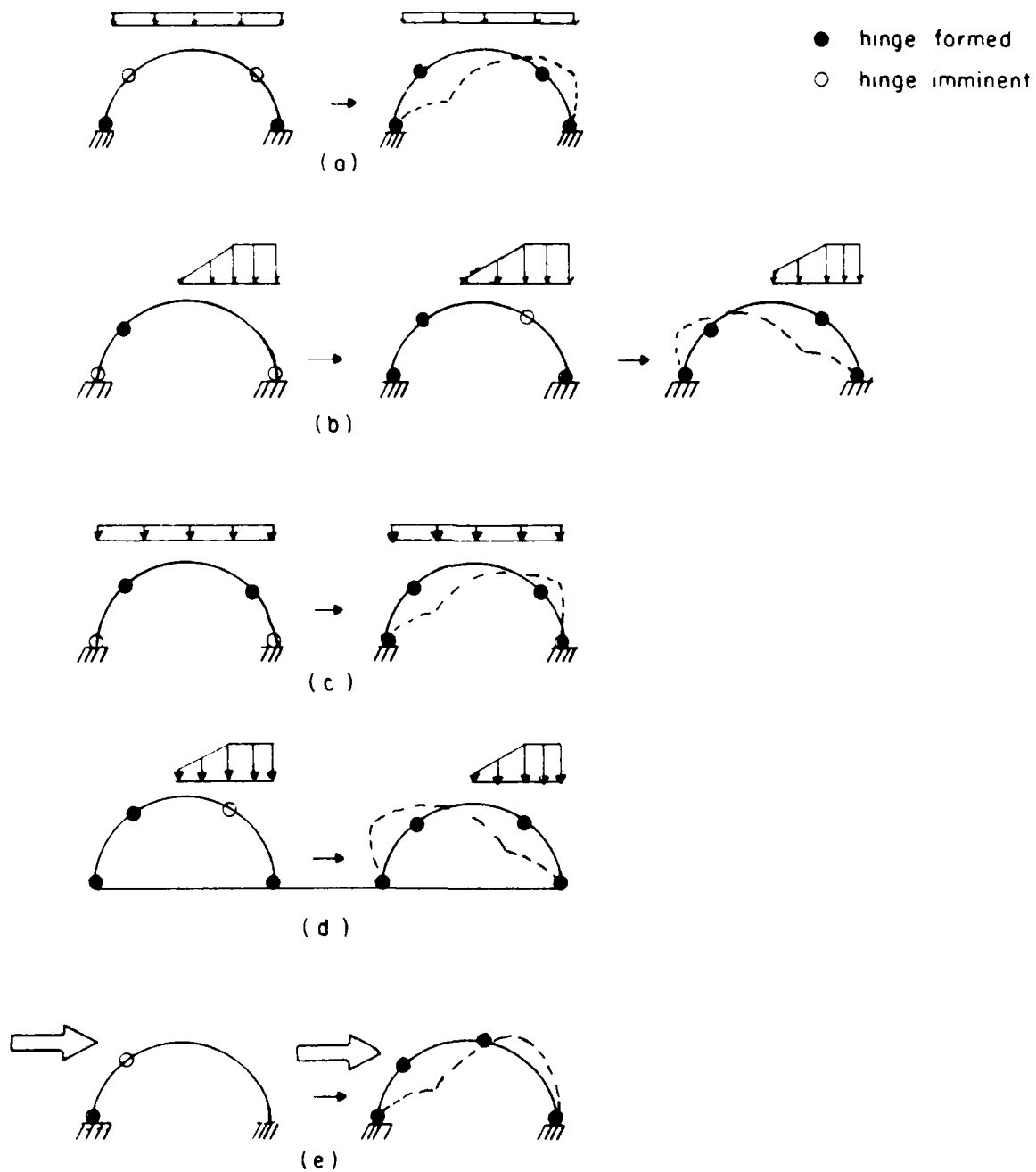


Figure 26. Collapsing mechanisms for the intermediate (a-b) and the large (c-e) buildings, under balanced (a,c), unbalanced (b,d), and wind loading (e).

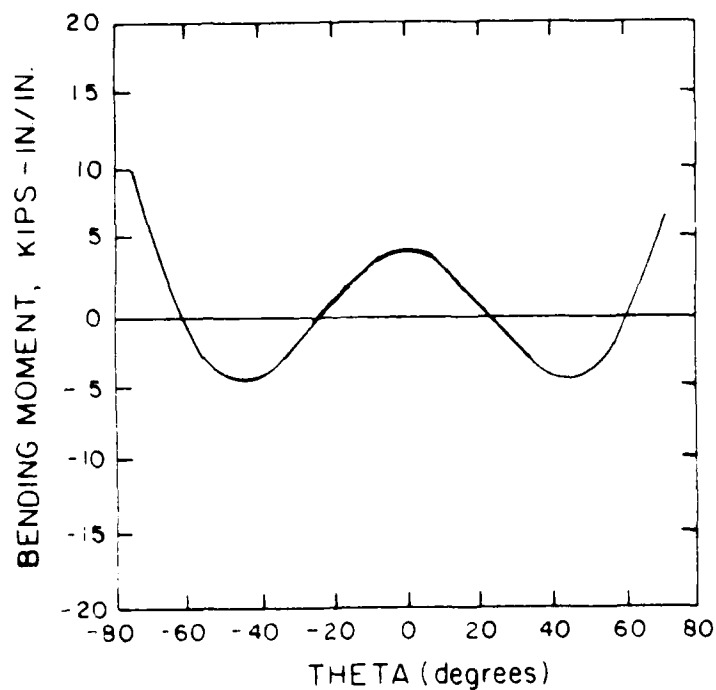


Figure 27. Moment distribution in the large building under the reference balanced snow loading.

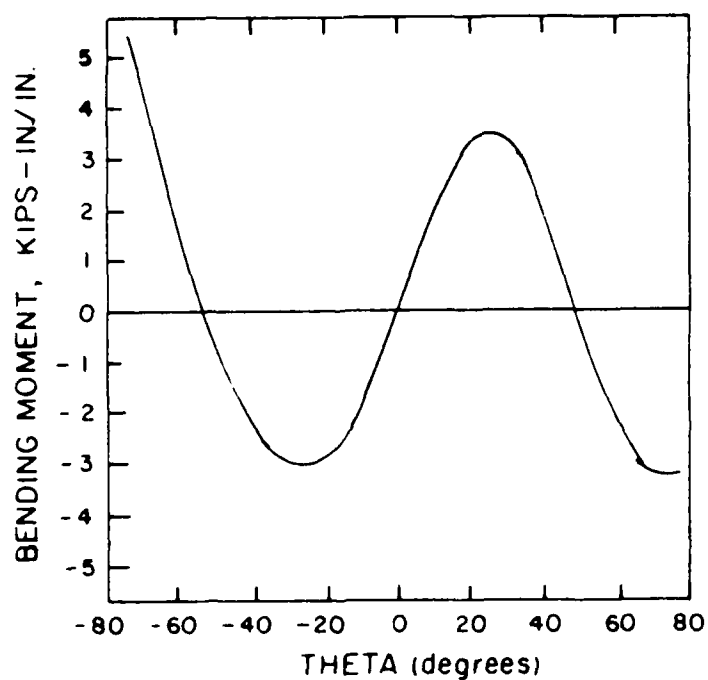


Figure 28. Moment distribution in the intermediate building under the reference unbalanced snow loading.

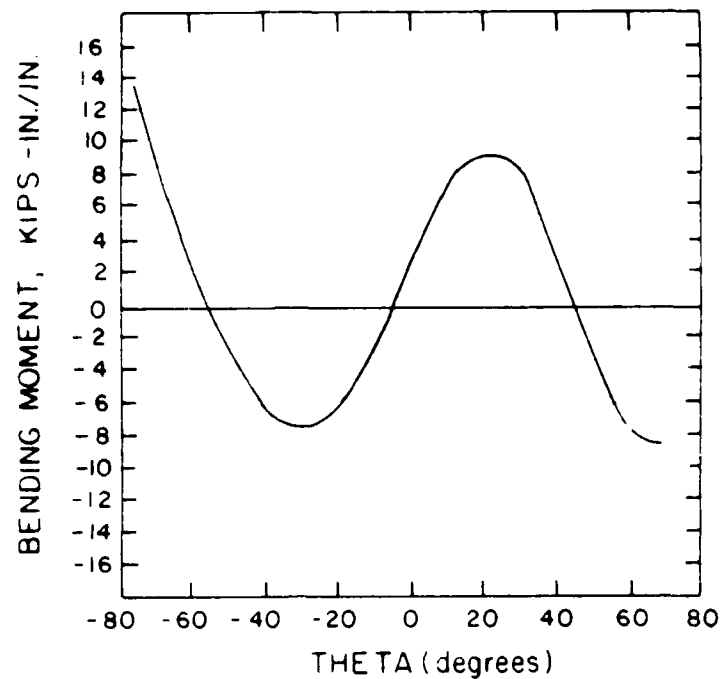


Figure 29. Moment distribution in the large building under the reference unbalanced snow loading.

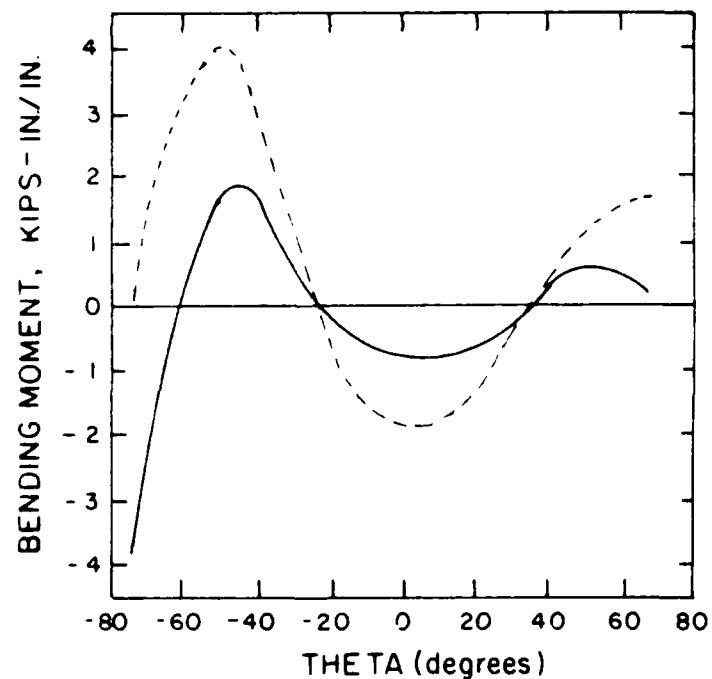


Figure 30. Moment distribution in the large building under the reference wind loading. (Dashed line corresponds to the moment distribution after the formation of the first hinge at the windward base of the structure.)

7 CONCLUSIONS

The collapse loads of corrugated-steel, barrel-type shells, under snow and wind loading conditions were determined in this study. The effect of local buckling was found to be critical in determining the mode of failure and the corresponding collapse loads. The orthotropy introduced by the geometry of the panels results in a significant increase of the bending rigidity of the structures. As a result, high bending moments develop within the structure under any type of loading. This, in turn, results in local buckling of the ridge-web section of the panels, under a critical positive moment field, or in local buckling of the flange of the panels, under a critical negative moment field. Local buckling is shown to govern the ultimate loading of these structures through the formation of collapsing mechanisms. The critical positive and negative moment fields under which hinges are formed determine the bounds to the critical loads which will create the collapsing mechanisms. Overall buckling was not found to be a design consideration for this particular type of structure. With a different profile of the panel yielding a lower degree of orthotropy, overall buckling could become critical for large building.

In regions where the design snow load is heavy, wind is also expected to be an important design factor. The corresponding combination of snow and wind loading, referred as unbalanced snow loading, governs the ultimate capacity of these buildings. The ultimate unbalanced ground snow load is 35 psf for the intermediate building (50 by 18 ft high and 14 psf for the large building (72 by 26 ft high). Note that these ultimate loads are conservative (lower limits).

In cases where snow is heavy but the structure is protected against the wind by technical or physical means (e.g., walls, trees), the balanced snow load governs the ultimate capacity of these structures. The ultimate balanced ground snow load is found to be 77 psf and 30 psf for the intermediate and large buildings, respectively. Again, these values are the lower limits of the ultimate load, thus they are conservative. The above results imply that protection against the wind could make a significant difference in the ultimate design load of these structures.

In most regions, whether or not snow load is considerable, wind load is always a design consideration, especially for large buildings. The ultimate wind load is found to correspond to a critical wind velocity with a lower bound of 60 to 68 mph and an upper bound of 74 mph for the large building. For the intermediate building these limits become 87 to 102 mph and 110 mph, respectively. Obviously, for smaller buildings, wind load will not be a design factor.

Comparing these ultimate loads to the design loads given by the manufacturer,²² one concludes that whereas these structures operate safely under snow load, they may be unsafe under wind load, depending on the building size. Thus, under the general assumptions of this analysis, the intermediate size building exhibits a factor of safety in the vicinity of one for wind loading, while the large size building has a factor of safety of less than one. Here it should be emphasized that the ultimate loads obtained in the present study are based on the assumption of a long structure (e.g., length/radius > 4). This suggests that for a medium length structure, where the effect of the end walls is not negligible, the ultimate loads determined here should be considered conservative. In addition, assumptions related to the quasistatic analysis for wind loading (e.g.,

²² K-Span.

exposure: see Chapter 2) may also contribute to a different actual wind pressure distribution and so to a different ultimate wind load velocity. The assumptions made in the present study are considered, for most cases, to be conservative.

Because of the rather low safety factor of the larger size buildings under wind loading, as determined in this analysis, it is suggested that further research be performed to determine the actual building response under wind loading.

METRIC CONVERSION FACTORS

$$1 \text{ ft} = 0.305 \text{ m}$$

$$1 \text{ sq ft} = 0.093 \text{ m}^2$$

$$1 \text{ in.} = 25.4 \text{ mm}$$

$$1 \text{ mph} = 1.61 \text{ km/hr}$$

$$1 \text{ psf} = 47.88 \text{ Pa}$$

$$1 \text{ ksi} = 6.895 \text{ MPa}$$

$$1 \text{ lb-in./in.} = 4.448 \text{ N}$$

REFERENCES

- ANSI Standard A58.1, *Minimum Design Loads for Buildings and Other Structures* (American National Standards Institute, Inc., NY, 1982).
- Bathe, K. J., *A Finite Element Program for Automatic Dynamic Incremental Nonlinear Analysis*, Report 82448.1 (Acoustics and Vibration Laboratory, Department of Mechanical Engineering, Massachusetts Institute of Technology, Cambridge, MA, 1975 [rev. 1978]).
- Briassoulis, D., "Analysis of the Behavior of Steel Silos Under Wind Loading," Ph.D. Dissertation, University of Illinois, Urbana, 1985.
- Briassoulis, D., "Equivalent Orthotropic Properties of Corrugated Sheets," *International Journal of Computers and Structures*, Vol 23, No. 2 (1985), pp 129-138.
- Billington, D. P., *Thin Shell Concrete Structures*, 2nd ed. (McGraw-Hill, NY, 1982).
- El-Atrouzy, M. N., and G. Abdel-Sayed, "Prebuckling Analysis of Orthotropic Barrel-Shells," *American Society of Civil Engineers Proceedings, Journal of the Structural Division*, Vol 104, ST11 (1978), pp 1775-1786.
- K-Span, *Metal Building Data Manual* (G. A. Kundson Ltd., Washington, DC).
- Lopez, L. A., "FINITE: An Approach to Structural Mechanics System," *International Journal of Numerical Methods in Engineering*, Vol 11 (1977), pp 851-866.
- Newberry, C. W. and K. J. Eaton, *Wind Loading Handbook* (Building Research Station, HMSO, London, 1975).
- Parish, H., "A Critical Survey of the Nine-Node Degenerated Shell Element With Special Emphasis on Thin Shell Application and Reduced Integration," *Computer Methods in Applied Mechanical Engineering*, Vol 20 (1979), pp 323-350.
- Sachs, P., *Wind Forces in Engineering*, 2nd ed. (Pergamon Press, 1977).
- Timoshenko, S. P., and J. M. Gere, *Theory of Elastic Stability*, 2nd ed. (McGraw-Hill, NY, 1961).

USA-CERL DISTRIBUTION

Chief of Engineers

ATTN: Tech Monitor
ATTN: CEIM-SL (2)
ATTN: CECC-P
ATTN: CECW
ATTN: CECW-0
ATTN: CECW-P
ATTN: CEEC
ATTN: CEEC-C
ATTN: CEEC-E
ATTN: CERD
ATTN: CERD-C
ATTN: CERD-M
ATTN: CERM
ATTN: DAEN-ZCE
ATTN: DAEN-ZCF
ATTN: DAEN-ZCI
ATTN: DAEN-ZCM
ATTN: DAEN-ZCZ

FESA, ATTN: Library 22060
ATTN: DET III 79906

US Army Engineer Districts
ATTN: Library (41)

US Army Engineer Divisions
ATTN: Library (14)

AMC - Dir., Inst., & Serve
ATTN: DEH (23)
ATTN: AMCEN-A

FORSCOM
FORSCOM Engr, ATTN: AFEN-DEH
ATTN: DEH (23)

TRADOC
HQ, TRADOC, ATTN: ATEN-DEH
ATTN: DEH (19)

CRREL, ATTN: Library 03755

WES, ATTN: Library 39180

NCEL
ATTN: Library, Code L08A 93043

Defense Technical Info. Center 22314
ATTN: DDA (2)

END

FEB.

1988

DTic